J. Fluid Mech. (1992), *vol.* 243, *pp.* 489–518
Printed in Great Britain

Shear flow over a wall with suction and its application to particle screening

By WANG-YI WU[1]†, SHELDON WEINBAUM[2]‡ AND ANDREAS ACRIVOS[1]

[1]The Levich Institute, The City College of the City University of New York, New York, NY 10031, USA

[2]Department of Mechanical Engineering, The City College of The City University of New York, New York, NY 10031, USA

(Received 14 August 1991)

In this paper, an extension of Miyazaki & Hasimoto's (1984) Green function for the slow flow created by a point force of arbitrary direction above an infinite plane wall with a circular hole was used to formulate a set of boundary-integral equations for the motion, at low Reynolds and Stokes numbers, of a finite rigid sphere in a simple shear flow with suction past an infinite wall containing a circular side hole. The equations were solved numerically by discretizing the surface of the sphere into a finite number of elements and then using a constant-density approximation for the unknown surface force distribution and a boundary collocation technique to satisfy the no-slip boundary condition at the centre of each element. Numerical tests and comparisons with available exact and numerical results show that convergence to three or four significant figures can be achieved for all the 21 independent unknown force and torque coefficients. Numerical values for these coefficients were obtained throughout the flow field for sphere–hole radii ratios of $\frac{1}{10}$, $\frac{1}{4}$, $\frac{1}{2}$, $\frac{3}{4}$ and 1, and the neutrally buoyant velocities and trajectories of individuals spheres were then computed for a range of initial upstream positions, and for various values of a suction parameter defined in Yan *et al.* (1991*a*) which refers to the relative strengths of the suction and shear flows. In turn, these trajectories were used to map out the particle capture tube and its upstream cross-section and thereby determine the particle screening effect, one of the underlying mechanisms responsible for the well-known exit concentration defect observed when particles enter a side pore. The other mechanism, the fluid skimming effect due to the presence of a particle-free layer on the upstream wall, was considered recently in a companion paper (Yan *et al.* 1991*a*). It is shown here that the fluid skimming effect provides a lower bound for this concentration defect under the conditions of this analysis. The theoretical predictions exhibit features that are qualitatively similar to the experimental observations of the hematocrit (red cell) defect in the microcirculation, although the dilute suspension limit considered herein is well below the observed hematocrit in the microcirculation and the particles are modelled as rigid spheres.

1. Introduction

The entrance flow problem for the motion of a sphere in a simple shear flow past a small hole with suction in an infinite plane wall has important applications in

† On leave from Department of Mechanics, Peking University, Beijing, P.R. China 100871.
‡ To whom correspondence should be addressed.

fluidization technology, through flow filters and the blood flow in the microcirculation. In the microcirculation, it well known from numerous laboratory experiments with small glass tubes and in various experiments with microvessels (Cokelet 1976; Chien, Usami & Skalak 1984; Gaehtgens & Papenfuss 1979; Lipowsky 1986; Pries, Ley & Gaehtgens 1986) that the discharge hematocrit H_D, defined as the fraction of red cells in blood, can be significantly lower than the feed hematocrit H_F in the upstream reservoir of the parent microvessel. Two basic mechanisms are believed to be responsible for this hematocrit defect: (i) the plasma skimming effect originating from the cell-free layer near the wall, and (ii) the particle screening effect caused by the deviation of the cell trajectories from the corresponding fluid streamlines due to the hydrodynamic interaction of the particles with the entrance geometry of the side branch. Recently, a simplified approximate three-dimensional theory was proposed by Yan, Acrivos & Weinbaum (1991*a*) to quantitatively analyse the fluid skimming effect at low Reynolds numbers for a dilute suspension of rigid spheres in a simple shear flow with suction past a side pore in a plane wall. This analysis was then generalized by the same authors (Yan, Acrivos & Weinbaum 1991*b*) to provide a first evaluation of plasma skimming at microvascular bifurcations for parent microvessels with an upstream Poiseuille flow. In the present paper the results of a comprehensive and rigorous three-dimensional numerical investigation are presented for the hydrodynamic interaction, at low Reynolds and Stokes numbers, of a finite rigid sphere with a circular orifice when the sphere undergoes a general rigid body motion in the presence of a combined shear flow and Sampson flow. Twenty one hydrodynamic force and torque coefficients were obtained numerically for spheres whose dimensionless radius scaled relative to that of the orifice is $\frac{1}{10}$, $\frac{1}{4}$, $\frac{1}{2}$, $\frac{3}{4}$ and 1 respectively. To the best of our knowledge values for many of these coefficients are presented here for the first time. These results are then utilized to determine the neutrally buoyant particle velocity, the particle capture tube cross-section far upstream of the hole and the particle screening effect. Although the present analysis is restricted to dilute suspensions which are well below the blood hematocrit in the microcirculation *in vivo*, the theoretical predictions exhibit the same qualitative trends as the experimental measurements.

As already discussed by Yan *et al.* (1991*a*), since the Reynolds numbers for the flow in the capture tube and through the pore are $O(Q^{\frac{2}{3}}\beta^2 Re_b)$ and $O(Q\beta^2 Re_b)$, respectively, where β is the ratio of the sidepore radius c to the main tube radius b, $2\pi Q$ is the non-dimensional volumetric fluid flux into the pore scaled with the wall shear rate in the main tube and the pore radius c, and Re_b is the Reynolds number in the feed tube, the entrance problem can be considered as a Stokes flow even if Q is greater than $O(1)$ and the Reynolds number of the main tube flow is greater than unity provided that $\beta \ll 1$. On the other hand, if $Re_b \ll 1$, as is the case in the microcirculation, no restriction on β is required.

On account of the linearity of the Stokes equations, the motion of a neutrally buoyant sphere in the vicinity of a circular orifice due to the action of a Sampson flow and the corresponding motion arising from the presence of a shear flow can be determined separately and then superimposed. The resulting motion is fully three-dimensional without planar symmetry. One can, however, rotate the Cartesian coordinate system with its origin at the centre of the orifice so as to position the centre of the sphere onto an (x, z)-plane, so that the incoming shear flow will now be inclined relative to this plane. In turn, this shear flow can be split into two parts, one parallel and the other perpendicular to the (x, z)-plane. These two flow components will be referred to henceforth as shear flow 1 and shear flow 2, respectively (cf.

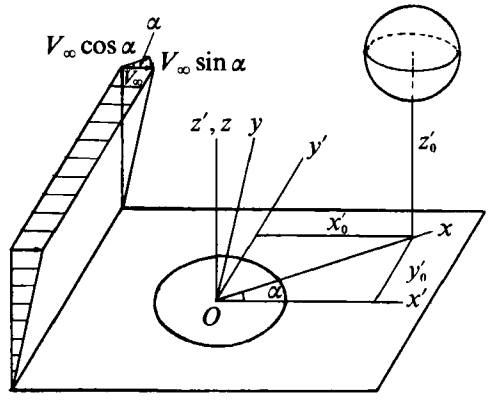

FIGURE 1. The various Cartesian coordinate systems.

figure 1). Consequently, the three-dimensional hydrodynamic interaction problem just described can be treated as the superposition of nine simpler flows: (1, 2, 3) the translation of the sphere in the x-, y- and z-directions in a quiescent fluid; (4, 5, 6) the rotation of the sphere about the x-, y- and z-axes in an otherwise quiescent fluid; (7) a Sampson flow past a stationary sphere; (8) shear low 1 past a stationary sphere; and (9) shear flow 2 past a stationary sphere. Furthermore, flows 1, 3, 5, 7 and 8 are symmetric while flows 2, 4, 6 and 9 are antisymmetric with respect to the (x, z)-plane, and hence the total number of unknown resistance coefficients that need to be determined is reduced by one half.

Although a variety of solutions for the motion of a sphere in the presence of an infinite plane wall at low Reynolds number have appeared in the literature (Brenner 1961; O'Neill 1964; Goldman, Cox & Brenner 1967*a b*), no information was available until relatively recently regarding the hydrodynamic resistance of a sphere moving in the vicinity of a pore entrance. Consequently, in the absence of the necessary data for the hydrodynamic force and torque coefficients, many investigators assumed that the particle velocity of a sphere approaching the pore was equal to that of the fluid surrounding it. This assumption was used extensively in the past in theoretical studies of aerosol filtration and the collection efficiency of nuclepore filters. The first studies which examined the pore entrance interaction were for a point force. Specifically, Davis, O'Neill & Brenner (1981) and Davis (1983) derived the axisymmetric solution for a point force moving toward a circular orifice along its centreline and obtained the force and torque correction factors for a sphere of small size, correct to the third order in a, the ratio of the sphere radius to that of the orifice. This same problem for three-dimensional motion was treated subsequently by Miyazaki & Hasimoto (1984) who constructed the closed form solution for a point force located anywhere along the (x, z)-plane and moving in an arbitrary direction above an infinite thin plane wall with a circular hole and then used it to determine the force and torque acting on a small sphere to first order in a. On the other hand, Dagan, Weinbaum & Pfeffer (1982) were the first to examine the axisymmetric orifice interaction problem for a sphere of finite size. These authors constructed different series solutions of the Fourier–Bessel type for each half-space and matched the solutions for the velocity and stress in the plane of the orifice by solving a pair of integral equations. Their solution, however, precludes the case where the sphere partially enters the orifice. The solution for a finite sphere in a Sampson orifice flow was then extended by Yan *et al.* (1987) to the corresponding three-dimensional

motion in which the sphere centre is located in a plane containing the orifice centreline. The latter authors introduced a combined multipole-series representation and integral-equation method for satisfying the no-slip conditions on the sidewall of the orifice with a boundary collocation technique applied on the surface of the sphere. Owing to the excessive computational time required, however, these authors evaluated numerically the twelve hydrodynamic force and torque coefficients only for $a = \frac{1}{2}$. Recently, Gavze (1990) employed a boundary-integral-equation method that utilized Blake's (1971) solution for the Green's function for a point force moving near an infinite plane wall. By constructing two different solutions for the upper and lower half-spaces and requiring that the velocity and the stress force be continuous, Gavze computed some limited numerical results for spheres and ellipsoids in a Sampson flow. As was the case with the method by Dagan *et al.* (1982), Gavze's technique has the disadvantage that the sphere cannot intersect the plane of the hole.

In two earlier studies, the hydrodynamic force and torque coefficients described above for a finite sphere in a Sampson flow were used to examine the deviation of the particle trajectories from the corresponding fluid streamlines as a spherical particle approaches a pore entrance. In Yan, Weinbaum & Pfeffer (1986), an approximate three-dimensional theory was developed for describing the fine structure of osmosis at the entrance to a circular membrane pore where the hydrodynamic interaction produces a three-dimensional standing concentration gradient at the pore entrance. The second application examined the impaction of spherical particles at the entrance to a pore at both zero and non-zero Stokes numbers, defined as the ratio of particle inertia to viscous forces (Dagan, Weinbaum & Pfeffer 1983; Wang *et al.* 1986), as well as the collection efficiency of nuclepore filters (Kao *et al.* 1988). Although, in both applications, the particle trajectories will in general deviate from the fluid streamlines on account of both their inertia and their interaction with the pore entrance, all the particles will eventually enter the pore, if forces of molecular origin are neglected. On the other hand, the present application for fluid and particle flow into a side branch from a shear layer differs fundamentally from the zero-Stokes-number solutions referred to above in that, now, there exist distinct particle and fluid capture tubes. These, in general, will not coincide far upstream, the deviation depending on the particle size and on the ratio of the magnitude of the side flux to the strength of the shear flow.

To determine the particle trajectories that form the boundaries of the particle capture tube, several new problems are considered herein for the first time. These include the hydrodynamic resistance of a sphere translating in the y-direction or rotating about the x- and z-axes, and shear flows 1 and 2 past a stationary sphere. Previous numerical results in Yan *et al.* (1987) and Gavze (1990) were only for a sphere having a radius one half that of the orifice, and none were for the case in which the sphere intersects the orifice plane and its centre is located off the pore axis. Finally, the conflicting results for several of the resistance coefficients given by Yan *et al.* (1987) and by Gavze (1990) needed to be resolved.

In the present study we shall apply the boundary-integral-equation method of Youngren & Acrivos (1975) using an extension of the Green's function developed by Miyazaki & Hasimoto (1984) for a point force moving either parallel or perpendicular to an infinite wall with a hole. The disturbance flow produced by the sphere and the plane wall with a hole is then expressed as a surface integral of a single-layer potential multiplied by an unknown density function which represents the stress force on the boundary surface. This method can also be applied to the case where the

sphere intersects the orifice opening. Although, in general, the expression for the disturbance flow also contains a double-layer potential, the contribution of the latter to the disturbance flow vanishes identically for rigid particle motion. The mathematical formulation of the problem and the boundary-integral-equation technique will be presented in §2, while, in §3, the convergence characteristics of the method will be examined as it applies to the calculation of the various resistance coefficients. It will be shown that convergence to three or four significant figures can be achieved for all the resistance coefficients, using a maximum of 11×11 elements on a half-sphere surface for $z_0/a \geqslant 1.1$, with z_0 denoting the distance of the centre of the sphere from the plane, except for the extreme cases where the sphere is quite close to the rim of the hole, where 12×12 elements are required to achieve convergence to three digits. The numerical results are compared with: (i) the exact solutions in the limiting case of a vanishing hole; (ii) the numerical solution of the axisymmetric motion of the sphere along the orifice centre line; (iii) the approximate solutions for a sphere of small size; (iv) the results of Yan *et al.* (1987) and Gavze (1990) for $a = \frac{1}{2}$. Results will be presented for all twenty-one independent resistance coefficients for $a = \frac{1}{10}, \frac{1}{4}, \frac{1}{2}, \frac{3}{4}$ and 1.

As described in §4, these force and torque coefficients were then used to calculate, for zero Stokes numbers, the velocity of a neutrally buoyant sphere at any point in the flow field, and thereby the sphere trajectories, the particle capture tube shapes and finally the particle screening effect that occurs at the entrance to the pore. The motion of those particles which impact the pore edge was also examined and, as will be shown, there exists a critical curve which separates the trajectories of those spheres which roll into the hole and those which are deflected downstream by the surrounding fluid. The shape of this curve depends on Q and on a. Some concluding remarks and a brief discussion of the qualitative features of these results as related to the discharge hematocrit defect are given in §5.

2. Formulation

Consider the arbitrary motion of a sphere in the presence of an infinite plane wall with a circular hole of unit radius, and under the action of an external flow consisting of a superposition of a Sampson flow and a simple shear flow. This simplified flow geometry also constitutes a reasonable approximation of a channel flow with a finite-length pore or of a flow in a tube with a side pore where the radius of the parent tube is large enough for its curvature to be neglected. We require that $\beta \ll 1$ *or* $Re_b \ll 1$, as mentioned in the introduction, so that the Stokes flow approximation will be valid. Furthermore, it is shown in Yan *et al.* (1991*a*), that the streamline pattern using Sampson's solution for the suction flow components provides a very good approximation to Tutty's (1988) finite-difference solution for pores of finite length. Cartesian coordinates (x', y', z') are introduced with the origin at the centre of the pore opening and the z'-axis pointing upwards along the pore axis (figure 1). The flow far from the pore opening is described by the superposition of a Sampson flow and a simple shear flow along the wall in the x'-direction.

Suppose next that the sphere centre is located at any position (x_0', y_0', z_0'). In this coordinate system the flow is fully three-dimensional without any symmetry. But, by rotating the Cartesian coordinates about the z'-axis and transforming them into a new coordinate system (x, y, z), we are able to place the centre of the sphere on the (x, z)-plane with coordinates $(x_0, 0, z_0)$. This coordinate transformation is given by

$$x = x' \cos\alpha + y' \sin\alpha, \tag{2.1}$$

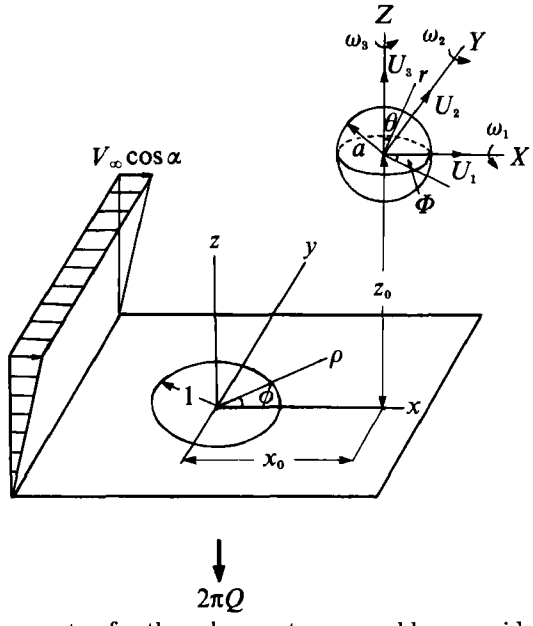

FIGURE 2. Flow geometry for the sphere entrance problem considered in this study.

$$y = -x' \sin\alpha + y' \cos\alpha, \tag{2.2}$$

$$z = z', \tag{2.3}$$

where $\alpha = \tan^{-1}(y_0'/x_0')$ is the angle between the x'- and x-axes. The shear flow is now split into two components: one parallel and one perpendicular to the (x, z)-plane which we shall refer to as shear flow 1 and shear flow 2 in that order. In the rotated x, y, z coordinate system the various flows will have planar symmetry or antisymmetry with respect to the (x, z)-plane, as noted previously. For mathematical convenience, cylindrical coordinates (ρ, ϕ, z) associated with the centre at the orifice opening are used. In addition, it is also convenient to introduce Cartesian coordinates (X, Y, Z), parallel to the rotated coordinates (x, y, z), and spherical coordinates (r, θ, Φ) fixed at the sphere centre (see figure 2). The relationships between the different coordinate systems are

$$X = r\sin\theta\cos\Phi, \quad Y = r\sin\theta\sin\Phi, \quad Z = r\cos\theta, \tag{2.4}$$

$$x = X + x_0, \quad y = Y, \quad z = Z + z_0 \tag{2.5}$$

and

$$\rho = (x^2+y^2)^{\frac{1}{2}}, \quad \phi = \tan^{-1}(y/x). \tag{2.6}$$

In general the sphere has a translational velocity vector $\boldsymbol{U}_0 = (U_1, U_2, U_3)$ and an angular vector $\boldsymbol{\Omega} = (\omega_1, \omega_2, \omega_3)$ whose components are along the (X, Y, Z) coordinates.

We next define the disturbance velocity and pressure fields by

$$\boldsymbol{V} = FCBI\ \boldsymbol{V}_1 - \boldsymbol{U}_\infty, \quad p = p_1 - p_\infty. \tag{2.7}$$

where $\boldsymbol{V}_1$ and p_1 are the actual fluid velocity and pressure while $\boldsymbol{U}_\infty$ and p_∞ refer to the velocity and pressure of the undisturbed flow in the absence of the sphere. The latter consists of a superposition of a Sampson flow and shear flows 1, 2 defined above. Therefore

$$\boldsymbol{U}_\infty = V_0^{\mathrm{s}}\,\boldsymbol{V}^{\mathrm{s}} + G\boldsymbol{V}^{\mathrm{sh}_1}\cos\alpha - G\boldsymbol{V}^{\mathrm{sh}_2}\sin\alpha, \tag{2.8}$$

$$p_\infty = V_0^{\mathrm{s}}\,p^{\mathrm{s}} + Gp^{\mathrm{sh}_1}\cos\alpha - Gp^{\mathrm{sh}_2}\sin\alpha, \tag{2.9}$$

where the superscripts s, sh_1, sh_{12} represent respectively the Sampson flow Oand shear flows 1 and 2, and G is the gradient of the shear flow at infinity. In addition, V_0^{s} is the fluid velocity of the Sampson flow in the plane of the pore at its centre:

$$V_0^{\mathrm{s}} = -3q/(2\pi), \tag{2.10}$$

where q is the volumetric fluid flux into the hole. Note that, for a hole of unit radius, (Happel & Brenner 1974)

$$q = \Delta p/(3\mu),$$

where Δp is the impressed pressure drop experienced by the fluid flowing through the aperture and μ is the fluid viscosity. The components of the Sampson velocity $\boldsymbol{V}^{\mathrm{s}}$ and pressure field p^{s}, normalized with V_0^{s} are (Happel & Brenner 1973)

$$\left.\begin{aligned} V_x^{\mathrm{s}} &= \frac{\lambda\zeta^2}{\lambda^2+\zeta^2}\left(\frac{1-\zeta^2}{1+\lambda^2}\right)^{\frac{1}{2}}\cos\phi, \quad V_y^{\mathrm{s}} = \frac{\lambda\zeta^2}{\lambda^2+\zeta^2}\left(\frac{1-\zeta^2}{1+\lambda^2}\right)^{\frac{1}{2}}\sin\phi, \\ V_z^{\mathrm{s}} &= \frac{\zeta^3}{\lambda^2+\zeta^2}, \quad p^{\mathrm{s}} = 2\mu\left[\frac{\lambda}{\lambda^2+\zeta^2}+\tan^{-1}\lambda\right], \end{aligned}\right\} \tag{2.11}$$

where λ, ζ are oblate spheroidal coordinates defined by

$$z = \lambda\zeta, \quad \rho = (\lambda^2+1)^{\frac{1}{2}}(1-\zeta^2)^{\frac{1}{2}} \quad (0 \leqslant \zeta \leqslant 1, \quad -\infty \leqslant \lambda \leqslant \infty). \tag{2.12}$$

The exact solution for the shear flow past a plane wall with a circular orifice was obtained by Hasimoto (1981) and, independently, by Smith (1987) and by Davis (1991) and the corresponding expressions for the velocity and pressure fields for shear flows 1 and 2 are given by (Davis 1991)

$$\left.\begin{aligned} V_x^{\mathrm{sh}_1} &= \frac{1}{3\pi}\frac{\lambda^2\zeta(1-\zeta^2)}{(\lambda^2+1)(\lambda^2+\zeta^2)}\cos 2\phi + \frac{\zeta}{\pi}\left[1-\lambda\tan^{-1}\frac{1}{\lambda}-\frac{\zeta^2}{3(\lambda^2+\zeta^2)}\right]+kz, \\ V_y^{\mathrm{sh}_1} &= \frac{1}{3\pi}\frac{\lambda^2\zeta(1-\zeta^2)}{(\lambda^2+1)(\lambda^2+\zeta^2)}\sin 2\phi, \\ V_z^{\mathrm{sh}_1} &= \frac{2}{3\pi}\frac{\lambda^2\zeta}{\lambda^2+\zeta^2}\left(\frac{1-\zeta^2}{1+\lambda^2}\right)^{\frac{1}{2}}\cos\phi, \end{aligned}\right\} \tag{2.13}$$

$$\left.\begin{aligned} p^{\mathrm{sh}_1} &= \frac{4}{3\pi}\mu\frac{\zeta}{\lambda^2+\zeta^2}\left(\frac{1-\zeta^2}{1+\lambda^2}\right)^{\frac{1}{2}}\cos\phi \\ V_x^{\mathrm{sh}_2} &= \frac{1}{3\pi}\frac{\lambda^2\zeta(1-\zeta^2)}{(\lambda^2+1)(\lambda^2+\zeta^2)}\sin 2\phi \\ V_y^{\mathrm{sh}_2} &= -\frac{1}{3\pi}\frac{\lambda^2\zeta(1-\zeta^2)}{(\lambda^2+1)(\lambda^2+\zeta^2)}\cos 2\phi + \frac{\zeta}{\pi}\left[1-\lambda\tan^{-1}\frac{1}{\lambda}-\frac{\zeta^2}{3(\lambda^2+\zeta^2)}\right]+kz, \\ V_z^{\mathrm{sh}_2} &= \frac{2}{3\pi}\frac{\lambda^2\zeta}{\lambda^2+\zeta^2}\left(\frac{1-\zeta^2}{1+\lambda^2}\right)^{\frac{1}{2}}\sin\phi, \\ p^{\mathrm{sh}_2} &= \frac{4}{3\pi}\mu\frac{\zeta}{\lambda^2+\zeta^2}\left(\frac{1-\zeta^2}{1+\lambda^2}\right)^{\frac{1}{2}}\sin\phi, \end{aligned}\right\} \tag{2.14}$$

where

$$k = \begin{cases} 1, & \text{for} \quad z \geqslant 0 \\ 0, & \text{for} \quad z < 0. \end{cases}$$

The governing equations for disturbance flow due to the sphere are then

$$\mu\nabla^2 \boldsymbol{V} = \nabla p, \quad \nabla\cdot\boldsymbol{V} = 0, \tag{2.15}$$

with boundary conditions on the sphere surface, the plane wall and at infinity, in that order,

$$\boldsymbol{V} = \boldsymbol{U}_0(\boldsymbol{x}) + \boldsymbol{\Omega}\times\boldsymbol{r}(\boldsymbol{x}) - \boldsymbol{U}_\infty(\boldsymbol{x}), \tag{2.16}$$

$$\boldsymbol{V} = 0, \tag{2.17}$$

$$\boldsymbol{V} = 0, \quad p = 0, \tag{2.18}$$

where $\boldsymbol{r}$ is the position vector (x_1, x_2, x_3) or (X, Y, Z) with origin at the sphere centre.

In what follows, we shall solve the boundary-value problem posed by (2.15)–(2.18) by means of the boundary-integral method, first proposed by Youngren & Acrivos (1975) for unbounded flows. But, instead of using the free space singularity or Stokeslet of Blake's (1971) solution, as was done by Gavze (1990), we shall apply the Green function developed by Miyazaki & Hasimoto (1984) for a point force moving in an arbitrary direction near a plane wall with a circular orifice. But, since the singularity derived by Miyazaki & Hasimoto is for the special case where the Stokeslet is located at the point $(y_1, 0, y_3)$ or $(x, 0, z)$, we first need to generalize their formulae to the general case where the Stokeslet moves in the j-direction and is located at an arbitrary point (y_1, y_2, y_3) or (x, y, z). Henceforth, these two notations will be used interchangeably. After some manipulations, the velocity and pressure at the field point (x_1, x_2, x_3) induced by this Stokeslet are found to be

$$\boldsymbol{G}^j(\boldsymbol{x},\boldsymbol{y}) = \frac{1}{8\pi\mu}\left[\boldsymbol{O}_j(L) - y_j\nabla L + \boldsymbol{O}_3(\Phi_j) + \boldsymbol{q}^j\right], \tag{2.19}$$

$$p^j(\boldsymbol{x},\boldsymbol{y}) = \frac{\partial L}{\partial x_j} + \frac{\partial \Phi_j}{\partial x_3} + \Pi^j, \tag{2.20}$$

where

$$\boldsymbol{O}_j(L) = x_j\nabla L - L\boldsymbol{x}_j. \quad \Phi_j = z\frac{\partial W}{\partial x_j} - (x_j - y_j)\frac{\partial W}{\partial z}, \tag{2.21a, b}$$

$$L = \tfrac{1}{2}(W - W^*), \quad H = \tfrac{1}{2}(W + W^*), \tag{2.21c, d}$$

$$W = \frac{1}{R}\left[1 + \frac{2}{\pi}\sin^{-1}\left(\frac{\cos\frac{1}{2}(\eta-\eta_0)}{\cosh(\frac{1}{2}\omega)}\right)\right], \quad W^* = \frac{1}{R^*}\left[1 + \frac{2}{\pi}\sin^{-1}\left(\frac{\cos\frac{1}{2}(\eta-\eta_0)}{\cosh(\frac{1}{2}\omega)}\right)\right], \tag{2.21e, f}$$

$$R = \frac{[2\cosh\omega - 2\cos(\eta-\eta_0)]^{\frac{1}{2}}}{MM_0}, \quad R^* = \frac{[2\cosh\omega - 2\cos(\eta+\eta_0)]^{\frac{1}{2}}}{MM_0}, \tag{2.21g, h}$$

$$M = (\cosh\xi - \cos\eta)^{\frac{1}{2}}, \quad M_0 = (\cosh\xi_0 - \cos\eta_0)^{\frac{1}{2}}, \tag{2.21i, j}$$

$$\cosh\omega = \cosh\xi\cosh\xi_0 - \sinh\xi\cosh\xi_0\cos(\phi-\phi_0), \tag{2.21k}$$

$$\boldsymbol{q}^1 = y_1\boldsymbol{q} - \mathrm{Re}(\boldsymbol{q}^*), \quad \boldsymbol{q}^2 = y_2\boldsymbol{q} - \mathrm{Im}(\boldsymbol{q}^*), \quad \boldsymbol{q}^3 = y_3\boldsymbol{q}, \tag{2.22a–c}$$

$$\boldsymbol{q} = C_L\boldsymbol{q}_L - C_H\boldsymbol{q}_H, \quad \boldsymbol{q}^* = (C_L\boldsymbol{q}_L^* - C_H\boldsymbol{q}_H^*)\,e^{i\phi_0}, \tag{2.22d, e}$$

$$C_L = (2/\pi)M_0\sin(\tfrac{1}{2}\eta_0), \quad C_H = (2/\pi)M_0\cos(\tfrac{1}{2}\eta_0),$$

$$\boldsymbol{q}_H = \tfrac{1}{2}\boldsymbol{O}_3(M_s\,\Psi), \quad \boldsymbol{q}_H^* = \tfrac{1}{2}\boldsymbol{O}_3(M_s\,\Psi^*), \tag{2.22f, g}$$

$$\boldsymbol{q}_L = \boldsymbol{q}_{L_0} + \tfrac{1}{6}\tau_0 \left\{ \boldsymbol{O}_\rho \left[M_s \left(\frac{1}{\tau} + \tau \right) \bar{\Psi} \right] + \frac{2}{\mathrm{i}} \left(\frac{1}{\tau} - \tau \right) M_s [\tau Z f(\tau Z) - \tau \bar{Z} f(\tau \bar{Z})] \, \boldsymbol{\phi}_0 \right.$$
$$\left. + \boldsymbol{O}_3 (M_c \, \bar{\Psi}) - 2 \boldsymbol{\nabla} (M_s \, \bar{\Psi}) \right\}, \quad (2.22h)$$

$$\boldsymbol{q}_L^* = \tau_0 \boldsymbol{q}_{L_0} + \tfrac{1}{6}\tau_0 \left\{ \boldsymbol{O}_\rho \left[M_s \left(\frac{1}{\tau} + \tau \right) \bar{\Psi}^* \right] + \frac{2}{\mathrm{i}} \left(\frac{1}{\tau} - \tau \right) M_s [\tau Z f(\tau Z) - \tau_0^2 \tau \bar{Z} f(\tau \bar{Z})] \, \boldsymbol{\phi}_0 \right.$$
$$\left. + \boldsymbol{O}_3 (M_c \, \bar{\Psi}^*) - 2 \boldsymbol{\nabla} (M_s \, \bar{\Psi}^*) \right\}, \quad (2.22i)$$

$$\boldsymbol{q}_{L_0} = \boldsymbol{O}_3 \left(\frac{\partial \boldsymbol{\Phi}_c}{\partial z} \right) + \boldsymbol{\nabla} \Phi_c, \quad \Phi_c = \frac{M_s}{M^2} + \frac{z}{\sqrt{2}} \tan^{-1} \frac{\sqrt{2} M_c}{M^2}, \quad \boldsymbol{O}_\rho(F) = \rho \boldsymbol{\nabla} F - F \boldsymbol{\rho}_0, \quad (2.22j\text{–}l)$$

$$\bar{\Psi} = \tau Z f(\tau Z) + \tau \bar{Z} f(\tau \bar{Z}), \quad \bar{\Psi}^* = \tau Z f(\tau Z) + \tau_0^2 \tau \bar{Z} f(\tau \bar{Z}), \quad (2.22m, n)$$

$$f(Z) = 1/(1 - \tau_0 Z), \quad \tau = \tanh \tfrac{1}{2}\xi, \quad \tau_0 = \tanh \tfrac{1}{2}\xi_0, \quad (2.22o\text{–}q)$$

$$Z = \mathrm{e}^{\mathrm{i}(\phi - \phi_0)}, \quad \bar{Z} = \mathrm{e}^{-\mathrm{i}(\phi - \phi_0)}, \quad \Psi = \tau_0 \bar{\Psi} + 1, \quad \Psi^* = \bar{\Psi}^* + \tau_0, \quad (2.22r\text{–}u)$$

$$M_s = M \sin(\tfrac{1}{2}\eta), \quad M_c = M \cos(\tfrac{1}{2}\eta), \quad (2.22v, w)$$

$$\boldsymbol{\rho}_0 = \boldsymbol{x}_1 \cos\phi + \boldsymbol{x}_2 \sin\phi, \quad \boldsymbol{\phi}_0 = -\boldsymbol{x}_1 \sin\phi + \boldsymbol{x}_2 \cos\phi, \quad (2.22x, y)$$

Here ξ, η, ϕ are toroidal coordinates related to ρ, z, ϕ by

$$\rho = \frac{\sinh\xi}{\cosh\xi - \cos\eta}, \quad z = \frac{\sin\eta}{\cosh\xi - \cos\eta}, \quad \phi = \phi,$$

and ξ_0, η_0, ϕ_0 are the toroidal coordinates of the Stokeslet. The expressions for Π^j in (2.20) will not be quoted here, because the pressure formulae will not be needed in the present study.

It is well known and easily verified that, for a rigid-body motion, the velocity field can be expressed solely in terms of a single-layer potential with the surface stress force $f_k(\boldsymbol{y})$ as its density no matter what the form of the undisturbed velocity $\boldsymbol{U}_\infty(\boldsymbol{x})$ as long as the latter satisfies the Stokes equations and has no singularities within the space enclosed by S_p, the surface of the particle. Thus, thus we have

$$V_i(\boldsymbol{x}) = \iint_{S_p} G_i^k(\boldsymbol{x}, \boldsymbol{y}) f_k(\boldsymbol{y}) \, \mathrm{d}S_y, \quad (2.23)$$

where $G_i^k(\boldsymbol{x}, \boldsymbol{y})$ is the Green's function due to a Stokeslet in the k-direction at point $\boldsymbol{y}$ given by (2.19) and (2.21), (2.22). The solution given by (2.23) satisfies the governing equation (2.15), the no-slip boundary conditions on the infinite sidewall of the hole and tends to zero at infinity. All that remains is to satisfy the no-slip boundary conditions on the surface of the sphere. This will eventually lead to a system of linear integral equations to be solved for the unknown density function f_k. Since the complexity of the Green's function appearing in (2.23) precludes an analytic solution, the system of equations will be solved numerically.

To this end, following the approach presented in Youngren & Acrivos (1975), the sphere surface is discretized into N elements $\Delta_m (m = 1, \ldots, N)$ and the unknown density function f_k within each element is approximated by a constant equal to the value of f_k at the centre of that element. Therefore, the number of unknowns $f_k(\boldsymbol{x}^m)$ is $3N$. Applying the boundary collocation technique, one then satisfies the no-slip

boundary conditions at the centre of each boundary element. The integral equation (2.23) is thus reduced to a system of $3N$ linear algebraic equations

$$\sum_{j=1}^{N} A_{ik}^{j}(\boldsymbol{x}^m) f_k(\boldsymbol{x}^j) = U_{\mathrm{p}_i}(\boldsymbol{x}^m), \tag{2.24}$$

with

$$A_{ik}^{j}(\boldsymbol{x}^m) = \iint_{\Delta_j} G_i^k(\boldsymbol{x}^m, \boldsymbol{y})\, \mathrm{d}S_y, \tag{2.25}$$

$$\boldsymbol{U}_{\mathrm{p}}(\boldsymbol{x}^m) = \boldsymbol{U}_0(\boldsymbol{x}^m) + \boldsymbol{\Omega} \times \boldsymbol{r}(\boldsymbol{x}^m) - \boldsymbol{U}_\infty(\boldsymbol{x}^m), \tag{2.26}$$

which can be solved by any matrix inversion technique. Finally, the expressions for the total force F_i and torque T_i exerted by the fluid on the sphere become, respectively,

$$F_i = \sum_{j=1}^{N} f_k(\boldsymbol{x}^j) \iint_{\Delta_j} \mathrm{d}S_y, \tag{2.27}$$

$$T_i = \sum_{j=1}^{N} f_k(\boldsymbol{x}^j) \iint_{\Delta_j} \epsilon_{ilk}\, y_l\, \mathrm{d}S_y. \tag{2.28}$$

By virtue of the linearity of the Stokes equation (2.15) and the corresponding boundary conditions (2.16)–(2.18), the general motion of a sphere in the vicinity of the orifice can then be decomposed into symmetric and antisymmetric components with respect to the (x, z)-plane. The symmetric component consists of five simpler flows: two pure translations with velocities $(1, 0, 0)$ and $(0, 0, 1)$ respectively, a pure rotation with angular velocity $(0, 1, 0)$ in an otherwise quiescent fluid, a Sampson flow with $V_0^{\mathrm{s}} = 1$ past a stationary sphere, and shear flow 1 with $G\cos\alpha = 1$ also past a stationary sphere. On the other hand, the antisymmetric component includes four simpler flows: a pure translation with velocity $(0, 1, 0)$ in an otherwise quiescent fluid, two corresponding pure rotations with angular velocities $(1, 0, 0)$ and $(0, 0, 1)$, respectively, and shear flow 2 with $G\sin\alpha = 1$ past a stationary sphere. These two flow problems are decoupled and, therefore, can be treated separately.

The hydrodynamic forces and torques on the sphere, which are related to the dimensionless resistance coefficients, the sphere velocity and the reference velocity of the Sampson flow and that of the shear flow can then be written as

$$\left.\begin{aligned} F_1 &= 6\pi\mu a(U_1 F_1^{\mathrm{t}_1} + U_3 F_1^{\mathrm{t}_3} + a\omega_2 F_1^{\mathrm{r}_2} + V_0^{\mathrm{s}} F_1^{\mathrm{s}} + Gz_0 F_1^{\mathrm{sh}_1}\cos\alpha),\\ F_3 &= 6\pi\mu a(U_1 F_3^{\mathrm{t}_1} + U_3 F_3^{\mathrm{t}_3} + a\omega_2 F_3^{\mathrm{r}_2} + V_0^{\mathrm{s}} F_3^{\mathrm{s}} + Gz_0 F_3^{\mathrm{sh}_1}\cos\alpha),\\ T_2 &= 8\pi\mu a^2(U_1 T_2^{\mathrm{t}_1} + U_3 T_2^{\mathrm{t}_3} + a\omega_2 T_2^{\mathrm{r}_2} + V_0^{\mathrm{s}} T_2^{\mathrm{s}} + \tfrac{1}{2}GaT_2^{\mathrm{sh}_1}\cos\alpha); \end{aligned}\right\} \tag{2.29}$$

$$\left.\begin{aligned} F_2 &= 6\pi\mu a(U_2 F_2^{\mathrm{t}_2} + a\omega_1 F_2^{\mathrm{r}_1} + a\omega_3 F_2^{\mathrm{r}_3} - Gz_0 F_2^{\mathrm{sh}_2}\sin\alpha),\\ T_1 &= 8\pi\mu a^2(U_2 T_1^{\mathrm{t}_2} + a\omega_1 T_1^{\mathrm{r}_1} + a\omega_3 T_1^{\mathrm{r}_3} - \tfrac{1}{2}GaT_1^{\mathrm{sh}_2}\sin\alpha),\\ T_3 &= 8\pi\mu a^2(U_2 T_3^{\mathrm{t}_2} + a\omega_1 T_3^{\mathrm{r}_1} + a\omega_3 T_3^{\mathrm{r}_3} - \tfrac{1}{2}GaT_3^{\mathrm{sh}_2}\sin\alpha), \end{aligned}\right\} \tag{2.20}$$

where $F_1^{\mathrm{t}_1}, \ldots, T_3^{\mathrm{sh}_1}$ are the twenty-seven dimensionless resistance coefficients related to the nine independent flows described above. The superscripts $\mathrm{t}_1, \mathrm{t}_3, \mathrm{r}_2, \mathrm{s}, \mathrm{sh}_1, \mathrm{t}_2, \mathrm{r}_1, \mathrm{r}_3, \mathrm{sh}_2$ represent these nine flows in sequence. In fact, only twenty-one of these coefficients are independent, because, on account of the Lorentz reciprocal theorem (Happel & Brenner 1973), twelve of the coefficients are related as follows:

$$\left.\begin{aligned} &F_1^{\mathrm{t}_3} = F_3^{\mathrm{t}_1}, \quad F_1^{\mathrm{r}_2} = \tfrac{4}{3}T_2^{\mathrm{t}_1}, \quad F_3^{\mathrm{r}_2} = \tfrac{4}{3}T_2^{\mathrm{t}_3},\\ &F_2^{\mathrm{r}_1} = \tfrac{4}{3}T_1^{\mathrm{t}_2}, \quad F_2^{\mathrm{r}_3} = \tfrac{4}{3}T_3^{\mathrm{t}_2}, \quad T_1^{\mathrm{t}_3} = T_3^{\mathrm{t}_1}. \end{aligned}\right\} \tag{2.31}$$

These relationships will also be used as one of the criteria to check the convergence and accuracy of the numerical method.

The corresponding linear algebraic equations for the nine basic flows, each having the same left-hand side, are constructed by replacing the right-hand side of (2.24) by $(1,0,0)$, $(0,0,1)$, $(0,-a\cos\theta,\ a\sin\theta\sin\Phi)$, $-\boldsymbol{V}^{\mathrm{s}}$, $-\boldsymbol{V}^{\mathrm{sh}_1}$, for the symmetric, and $(0,1,0)$, $(a\cos\theta,0,-a\sin\theta\cos\Phi)$, $(-a\sin\theta\sin\Phi,\ a\sin\theta\cos\Phi,0)$ and $-\boldsymbol{V}^{\mathrm{sh}_2}$ for the antisymmetric cases respectively. These equations, when solved, yield the above twenty-seven resistance coefficients.

In fact, the force and torque exerted on a stationary sphere by the incoming Sampson flow and by the two shear flows may be calculated directly using the density functions generated from the six independent translations and rotations of the rigid sphere without invoking the solution of the linear algebraic equations (2.24). For example, for the Sampson flow s and the translational motion t_1, the reciprocal theorem states that

$$\int_{S_{\mathrm{p}}} \boldsymbol{V}^{\mathrm{t}_1}\cdot\boldsymbol{\Pi}^{\mathrm{s}}\cdot\mathrm{d}\boldsymbol{S} = \int_{S_{\mathrm{p}}} \boldsymbol{V}^{\mathrm{s}}\cdot\boldsymbol{\Pi}^{\mathrm{t}_1}\cdot\mathrm{d}\boldsymbol{S},$$

where $\boldsymbol{\Pi}$ is the corresponding stress tensor. Therefore, in view of (2.29), we have that

$$F_1^{\mathrm{s}} = \frac{1}{6\pi a\mu V_0^{\mathrm{s}}}\left[\sum_{j=1}^{N}\iint_{S_j} f_i^{\mathrm{t}_1}(x^j)\cdot\boldsymbol{V}_1^{\mathrm{s}}\,\mathrm{d}S_{\mathrm{y}}\right],$$

where $f_i^{\mathrm{t}_1}$ is already known from the solution of the t_1 problem. Similar expressions can be written for $F_3^{\mathrm{s}}, T_2^{\mathrm{s}}, F_1^{\mathrm{sh}_1}, F_2^{\mathrm{sh}_2}$ etc. in (2.29) and (2.30). Of course, all of the dimensionless resistance coefficients are functions of the sphere radius as well as of the position of the sphere centre.

As noted above, in the Cartesian coordinate system (x,y,z), and with the sphere centre on the (x,z)-plane, the basic flows are either symmetric or antisymmetric about the (x,z)-plane. Then, if $P(x,y,z)$ and $P'(x,-y,z)$ are a pair of symmetric points about the (x,z)-plane, we have that

$$f_x(P) = f_x(P'),\quad f_z(P) = f_z(P'),\quad f_y(P) = -f_y(P') \text{ for the symmetric case}$$
$$f_x(P) = -f_x(P'),\quad f_z(P) = -f_z(P'),\quad f_y(P) = f_y(P') \text{ for the antisymmetric case}$$

In either case, one needs to evaluate the unknown density functions only over one-half the sphere surface. But since the computation time is approximately proportional to the square of the number of elements, this simplification greatly reduces the memory requirements and the CPU time.

For a sphere, a natural way of proceeding is to divide the surface of a half-sphere at $y \geqslant 0$ by choosing $N\times N$ elements with N equal intervals in both the θ- and ϕ-directions, and to employ a simple 4×4 composite Gaussian quadrature based on a one-dimensional corresponding formula to evaluate the two-dimensional integral (2.25). The error will decrease with increasing values of N. The numerical evaluation of the surface integrals encounters no difficulty when the integrand is regular, but if the element contains the point $\boldsymbol{x}^m$, the integral becomes singular at $\boldsymbol{x}^j = \boldsymbol{x}^m$. A procedure similar to that proposed by Youngren & Acrivos (1975) was therefore adopted. Specifically, the element was divided into two regions: one with a small area Δ_ϵ around $\boldsymbol{x}^m$ and the other being the remainder. Then, by approximating the surface of Δ_ϵ by the tangent plane at $\boldsymbol{x}^m$ with the small area replaced by a square of sides 2ϵ and transforming the coordinate system to a local polar one, we were able to evaluate the improper integrals analytically, even though the flow geometry was much more

complicated than in Youngren & Acrivos (1975). The details are given in the Appendix. The integration to be performed over the remaining surface is regular and was accomplished using 8×8 composite Gaussian formulae to achieve the required accuracy.

Our numerical experiments showed that for most values of z_0/a and for most of the resistance coefficients, the results are insensitive to the choice of ϵ in the range $0.01l \leqslant \epsilon l \leqslant 0.3l$, where l is the smaller side length of the rectangle Δ_m formed by the $N \times N$ elements. However, for some coefficients, for example, $F_3^{t_3}$ and $F_1^{t_3}$, the integration was found to be sensitive to ϵ, when the sphere was located near the plane wall. Numerical experience indicates, however, that, for each z_0/a in the range $1.1 \leqslant z_0/a \leqslant 2$ there exists an optimum value of ϵ in the sense that this choice of ϵ gives the best agreement with the known expressions for these coefficients far from the hole. Using this optimum value, the convergence process can be markedly accelerated. The optimum values of ϵ thus found are given in the Appendix.

The linear system of algebraic equations was solved by standard Gaussian elimination techniques. Since a considerable part of the computer time is spent in inverting the matrix A_{ik}^j, it is worthwhile to note that this matrix depends only on the particle geometry and is independent of both the form of the incoming flow velocity and of the particle motion. Thus, only a single matrix inversion is required for all the nine basic flows associated with the general motion of the sphere.

3. Numerical results

3.1. *Convergence and accuracy*

We first discuss the convergence and accuracy of the numerical method. For $a = \frac{1}{2}$, $x_0 = \frac{1}{4}$ and $z_0/a = \frac{3}{2}$, which is representative of a moderate sphere–orifice interaction, convergence to three or four significant digits was achieved for all coefficients using a maximum of 10×10 elements on the surface of the half-sphere. The six reciprocal identities (2.30) were also satisfied with a maximum relative error of less than 0.05%. To further test the convergence of the method, the strongest interaction position $x_0 = 1.0$, $z_0/a = 1.1$ ($a = \frac{1}{2}$) was selected, but even for this difficult case, two- or three-digit convergence was attained using a maximum of 12×12 elements. A similar degree of convergence was obtained for the reciprocal relations (2.31). On the other hand, when $z_0/a \geqslant 4$, only 8×8 elements were required to achieve three- or four-digit convergence.

Numerical tests of the solution accuracy were conducted for those cases where exact solutions or other numerical solutions were available for comparison. For example, as $x_0 \to \infty$, the present problem becomes identical to that of a translating and rotating sphere in the presence of a simple shear flow above an infinite wall plane. Hence, our solutions at $a = \frac{1}{2}$, $x_0 = 10$ were compared with the corresponding exact solutions given in Goldman *et al.*(1967*a*, *b*). Again, the two sets of coefficients were found to be identical to at least three-digits.

Many authors have considered two axisymmetric cases: a sphere moving along the orifice centreline in a quiescent fluid and a Sampson flow past a stationary sphere with its centre on the orifice axis. In tables 1 and 2 our values for the corresponding resistance coefficients $F_3^{t_3}$ and F_3^{s} are compared with those given by Yan *et al.* (1987), Davis (1983), Dagan *et al.* (1982) and Gavze (1990). Clearly, there is close agreement between all these results except for Davis' solution for a small sphere, which, as expected, deteriorates for $a \geqslant 1$. The present results agree especially well with Gavze's values for $F_3^{t_3}$ and with Davis' results when $a \leqslant \frac{1}{2}$.

z_0/a		$a=\frac{1}{10}$	$\frac{1}{2}$	1	5
2.0	(i)	−1.055	−1.488	−1.884	−2.124
	(ii)	−1.054	−1.426	−1.865	−2.119
	(iii)	−1.054	−1.484	−1.840	−1.998
	(iv)	−1.051	−1.392	−1.806	−2.120
	(v)	−1.055	−1.487	−1.871	−2.095
1.5	(i)	−1.053	−1.494	−2.184	−3.168
	(ii)	−1.052	−1.421	−2.104	−3.153
	(iii)	−1.053	−1.487	−2.086	−2.506
	(iv)	−1.050	−1.388	−2.033	−3.154
	(v)	−1.055	−1.494	−2.172	−3.106
1.1	(i)	−1.052	−1.469	−2.499	−8.17
	(ii)	−1.051	−1.395	−2.360	−8.47
	(iii)	−1.052	−1.459	−2.266	−2.84
	(iv)	−1.050	−1.377	−2.287	−8.94
	(v)	−1.056	−1.472	−2.489	−8.39

(i) present work, (ii) Yan *et al.* (1987), (iii) Davis (1983), (iv) Dagan *et al.* (1982), (v) Gavze (1990)

TABLE 1. A sphere translating along the orifice centreline in a quiescent fluid (comparison of the resistance coefficients for F_3^t)

z_0/a		$a=\frac{1}{10}$	$\frac{1}{2}$	1
2.0	(i)	1.007	0.685	0.361
	(ii)	1.007	0.652	0.359
	(iii)	1.007	0.701	0.458
	(iv)	1.004	0.627	0.328
1.5	(i)	1.023	0.843	0.579
	(ii)	1.022	0.798	0.568
	(iii)	1.023	0.820	0.824
	(iv)	1.021	0.776	0.483
1.1	(i)	1.033	0.961	0.768
	(ii)	1.033	0.912	0.753
	(iii)	1.032	0.885	1.068
	(iv)	1.031	0.906	0.640

(i) present work, (ii) Yan *et al.* (1987), (iii) Davis (1983), (iv) Dagan *et al.* (1982)

TABLE 2. Sampson flow past a stationary sphere with its centre on the orifice axis (comparison of the resistance coefficients for F_3^s)

z_0/a		$a=\frac{1}{10}$	$\frac{1}{4}$	$\frac{1}{2}$	$\frac{3}{4}$	1
1.0	(i)	−1.052	−1.156	−1.459	−1.946	−2.587
	(ii)	−1.051	−1.142	−1.386	−1.944	−2.457
0.5	(i)	−1.051	−1.145	−1.398	−1.918	−3.26
	(ii)	−1.050	−1.133	−1.336	−1.916	−3.332
0	(i)	−1.051	−1.140	−1.364	−1.858	—
	(ii)	−1.050	−1.129	−1.310	−1.777	—

(i) present work, (ii) Yan *et al.* (1987)

TABLE 3. Comparison of the resistance coefficients for F_3^t when $0 \leqslant z_0/a \leqslant 1.1$, $x_0 = y_0 = 0$

z_0/a		$x_0 = 0$	0.25	0.50	0.75	1.00	1.25	1.50	2.00
1.10	(i)	1.052	1.056	1.073	1.147	5.62	11.37	11.42	11.44
	(ii)	1.049	1.052	1.067	1.123	2.022	2.023	2.023	2.023
1.25	(i)	1.052	1.056	1.074	1.151	3.203	5.292	5.302	5.304
	(ii)	1.049	1.053	1.067	1.126	1.900	1.900	1.900	1.900
1.50	(i)	1.053	1.057	1.075	1.156	2.263	3.192	3.203	3.205
	(ii)	1.050	1.054	1.069	1.130	1.749	1.750	1.750	1.750
2.00	(i)	1.055	1.059	1.079	1.163	2.116	2.127	2.127	2.127
	(ii)	1.051	1.055	1.072	1.136	1.559	1.562	1.562	1.563
4.00	(i)	1.063	1.069	1.091	1.155	1.364	1.379	1.379	1.381
	(ii)	1.059	1.064	1.083	1.133	1.272	1.280	1.280	1.281
10.00	(i)	1.074	1.076	1.084	1.095	1.117	1.122	1.122	1.126
	(ii)	1.068	1.070	1.077	1.087	1.105	1.109	1.109	1.112

(i) present work, (ii) Miyazaki & Hasimoto (1984)

TABLE 4. The case of a small sphere (comparison of the resistance coefficients for $-F_3^{t_3}$ when $y_0 = 0$, $a = \frac{1}{10}$

As mentioned in the introduction, the technique employed by Dagan *et al.* (1982) and by Gavze (1990) fails where the sphere intersects the plane of the orifice, a case which is important in treating pore entrance phenomena such as the particle screening effect. In contrast, our solution method, as well as the technique proposed by Yan *et al.* (1987), can treat this case without difficulty. In table 3 typical results for $F_3^{t_3}$ are compared with those given by Yan *et al.* (1987) for $0 \leqslant z_0/a \leqslant 1.0$ along the axis of the orifice. It is seen that there is reasonable agreement between the two sets for all values of a. Similar agreement was obtained for F_3^{s}.

Using their point force solution, Miyazaki & Hasimoto (1984) derived the expressions for several resistance coefficients, correct to first order in the sphere radius a. It should be noted, though, that their formula for the x-component of the force, when the point force moves in the x-direction, is in error (Miyazaki & Hasimoto, 1984, p. 211, eq. (4.9). The correct expression for this force component is

$$\frac{1}{16\pi}\Bigg[M^4(-4+4\cos\eta)+M^2\left(9\frac{\pi-\eta}{\sin\eta}+10-10\cos\eta+8\cos^2\eta+\cos^3\eta\right)-8+2\cos^2\eta$$

$$+4\cos^3\eta+2\cos^4\eta+\frac{1}{M^2}(10-9\cos\eta-10\cos^2\eta+8\cos^3\eta+\cos^5\eta)$$

$$-\frac{6(1+\cos\eta)}{M^2}\sin^2\eta\left(\frac{4}{\cosh\xi+1}-2\right)$$

$$+4\frac{1-\cos\eta}{\cosh\xi+1}(M^6+M^4\cos\eta+M^2\sin^2\eta+\cos\eta\sin^2\eta)\Bigg].$$

Because of space limitations we shall compare our results for $F_3^{t_3}$ with those obtained by Miyazaki & Hasimoto (1984) only for $a = \frac{1}{10}$. As seen in table 4, the agreement is good only over the hole.

Our computed values for $F_3^{t_3}$, $F_1^{t_3}$ and $F_1^{r_2}$ for the planar symmetric case, in which the sphere with its centre lying in a plane that contains the pore centreline translates in the z-direction and rotates about the y-axis in a quiescent fluid, are compared in tables 5, 6 and 7 with the corresponding results in Yan *et al.* (1987) and in Gavze

z_0/a		$x_0 = 0$	0.50	0.75	1.00	2.00
10	(i)	1.125	1.125	1.125	1.126	1.126
	(ii)	1.123	1.123	1.123	1.123	1.123
	(iii)	1.125	1.100	1.100	1.100	1.100
4	(i)	1.327	1.334	1.341	1.350	1.374
	(ii)	1.322	1.329	1.336	1.344	1.367
	(iii)	1.300	1.300	1.300	1.300	—
2	(i)	1.488	1.585	1.707	1.855	2.116
	(ii)	1.487	1.585	1.705	1.848	2.089
	(iii)	1.426	1.450	1.550	1.650	—
1.5	(i)	1.494	1.676	1.977	2.440	3.191
	(ii)	1.494	1.682	1.985	2.449	3.125
	(iii)	1.421	1.5	1.7	2.0	—
1.1	(i)	1.469	1.750	2.530	5.99	11.38
	(ii)	1.472	1.766	2.606	6.226	10.92
	(iii)	1.395	1.6	1.9	—	—

(i) present work, (ii) Gavze (1990), (iii) Yan *et al.* (1987)

TABLE 5. The three-dimensional case when the sphere centre is located in the plane containing the hole centre (comparison of the resistance coefficients for $-F_3^{t_3}$, $a = \frac{1}{2}$)

z_0/a		$x_0 = 0$	0.2	0.4	0.6	0.8	1.0	1.2	1.4
2	(i)	0	0.0317	0.0615	0.0857	0.0985	0.0951	0.0771	0.0538
	(ii)	0	0.0314	0.0606	0.0838	0.0951	0.0904	0.0722	0.0497
	(iii)	0	0.0150	0.0200	0.0300	0.0350	0.0300	0.0200	0.0200
1.5	(i)	0	0.0523	0.1080	0.1667	0.215	0.220	0.168	0.0989
	(ii)	0	0.0524	0.1082	0.1661	0.2115	0.2118	0.1569	0.0899
	(iii)	0	0.0300	0.0500	0.0600	0.0600	0.0500	0.0400	0.0300
1.25	(i)	0	0.0631	0.1372	0.2336	0.352	0.418	0.304	0.147
	(ii)	0	0.0632	0.1384	0.2365	0.3535	0.4000	0.2781	0.1306
	(iii)	0	—	—	—	—	—	—	—
1.1	(i)	0	0.0683	0.154	0.285	0.520	0.823	0.540	0.200
	(ii)	0	0.0679	0.1562	0.2940	0.5446	0.7823	0.4807	0.1732
	(iii)	0	0.0400	0.0700	0.0800	0.0800	0.0600	0.0500	0.0400

(i) Present work, (ii) Gavze (1990), (iii) Yan *et al.* (1987)

TABLE 6. The three-dimensional case when the sphere centre is located in the plane containing the hole centre (comparison of the resistance coefficients for $F_1^{t_3}$, $a = \frac{1}{2}$)

(1990). Looking at table 5, we find that our values for $F_3^{t_3}$ agree with Gavze's to three digits, except for those very near the rim of the hole or near the plane wall. Poorer agreement is obtained for $F_3^{t_3}$ with Yan *et al.* (1987) especially for $z_0/a \leqslant 2$, with a maximum deviation of 25% at $x_0 = 0.75$ and $z_0/a = 1.1$. Also, the results in tables 6 and 7 for the cross-couple resistance coefficients $F_1^{t_3}$ and $F_3^{r_3}$ show good agreement with those given by Gavze, but can be as much as an order of magnitude higher than those reported in Yan *et al.* (1987). Hence, the latter are undoubtedly erroneous.

The convergence and accuracy tests just summarized convincingly demonstrate that the method has impressive convergence and accuracy characteristics even for the most extreme case where the sphere is either intersecting the plane of the orifice or interacting with the rim of the pore.

z_0/a		$x_0 = 0$	0.2	0.4	0.6	0.8	1.0	1.2	1.4
2	(i)	0	0.00676	0.0134	0.0193	0.0230	0.0230	0.0191	0.0136
	(ii)	0	0.006	0.013	0.018	0.021	0.020	0.017	0.012
	(iii)	0	0.000	0.006	0.010	0.010	0.010	0.006	0.004
1.5	(i)	0	0.0149	0.0317	0.0514	0.0709	0.077	0.0589	0.0338
	(ii)	0	0.015	0.031	0.049	0.065	0.068	0.050	0.028
	(iii)	0	0.000	0.010	0.020	0.040	0.040	—	—
1.25	(i)	0	0.0215	0.0488	0.0889	0.147	0.184	0.133	0.0603
	(ii)	0	0.023	0.049	0.087	0.139	0.167	0.1125	0.050
	(iii)	0	—	—	—	—	—	—	—
1.1	(i)	0	0.0265	0.063	0.127	0.262	0.443	0.287	0.09
	(ii)	0	0.029	0.065	0.126	0.256	0.438	0.238	0.076
	(iii)	0	0.005	0.015	0.040	0.080	0.120	—	—

(i) present work, (ii) Gavze (1990), (iii) Yan *et al.* (1987)

TABLE 7. The three-dimensional case when the sphere centre is located in the plane containing the hole centre (comparison of the resistance coefficients for $F_3^{r_3}$, $a = \frac{1}{2}$)

3.2. *Resistance coefficients*

Twenty one independent resistance coefficients were computed for a wide range of a, x_0 and z_0/a: $a = \frac{1}{10}, \frac{1}{4}, \frac{1}{2}, \frac{3}{4}, 1$; $x_0 = 0, \frac{1}{4}, \frac{1}{2}, \frac{3}{4}, 1, \frac{5}{4}, \frac{3}{2}$ 2, 10; $z_0/a = \frac{11}{10}, \frac{5}{4}, \frac{3}{2}$, 2, 4, 10. In addition, for the sphere intersecting the pore opening, the following values for the coordinates of the sphere centre were chosen: $x_0/b(z_0) = 0, \frac{1}{4}, \frac{1}{2}, \frac{3}{4}$; $z_0/a = 0, \frac{1}{4}, \frac{1}{2}, \frac{3}{4}, 1$, where the curve $x_0 = b(z_0) \equiv 1-a(1-z_0/a)^{\frac{1}{2}}$ represents the boundary of the particle-free layer. The six remaining resistance coefficients can be easily evaluated by making use of (2.31) which is derived from the reciprocal theorem. With 8×8, 9×9, 10×10 and 11×11 elements, the computation time required for one run was, respectively, 1:38, 2:30, 3:30, 5:41 minutes of CPU time on an IBM 3081.

We shall first present results for all the coefficients for $a = \frac{1}{2}$. To the best of our knowledge those for translation 2, rotation 1,3 and shear flow 1,2 are entirely new. Moreover, the values of the aforementioned resistance coefficients for the case in which the sphere intersects the pore opening and is located off the pore centreline are also new. Although data for the other four motions had been published previously by Yan *et al.* (1987) and by Gavze (1990), our results are still of interest because they are more accurate and reliable than those of Yan *et al.* and more complete than Gavze's.

Figure 3(*a–c*) shows plots of the dimensionless hydrodynamic force and torque coefficients $-F_1^{t_1}$, $-F_2^{t_2}$, $-F_3^{t_3}$ and $-T_1^{r_1}$, $-T_2^{r_2}$, $-T_3^{r_3}$ for a sphere of dimensionless radius $a = \frac{1}{2}$ as a function of x_0 and z_0/a. It is seen that these six curves are similar in shape, and that the influence of the orifice is largely confined to the region $x_0 \leqslant 1.5$ and $z_0/a \leqslant 2.0$ for this value of a. Also shown are the solutions of Brenner (1961) for the limiting case of an infinite plane wall. As expected, the sphere experiences a smaller resistance for both translation and rotation as it approaches the orifice and the minimum value of the corresponding coefficient lies on the centreline. In general, $T_i^{t_i}(x_0, z_0) \leqslant F_i^{t_i}(x_0, z_0)$ $(i = 1, 2, 3)$, and although the values of $F_2^{t_2}$ and $T_2^{r_2}$ are approximately equal to those of $F_1^{t_1}$ and $T_1^{r_1}$, respectively, they are not identical, except at $x_0 = 0$ and as $x_0 \to \infty$, because of the lack of symmetry between the motions in the x- and y-directions except for these limiting cases. We also note that the coefficient for translation normal to the wall, $F_3^{t_3}$, increases much more rapidly with increasing x_0 than $F_1^{t_1}$ and $F_2^{t_2}$, since the limiting solutions in the absence of the orifice

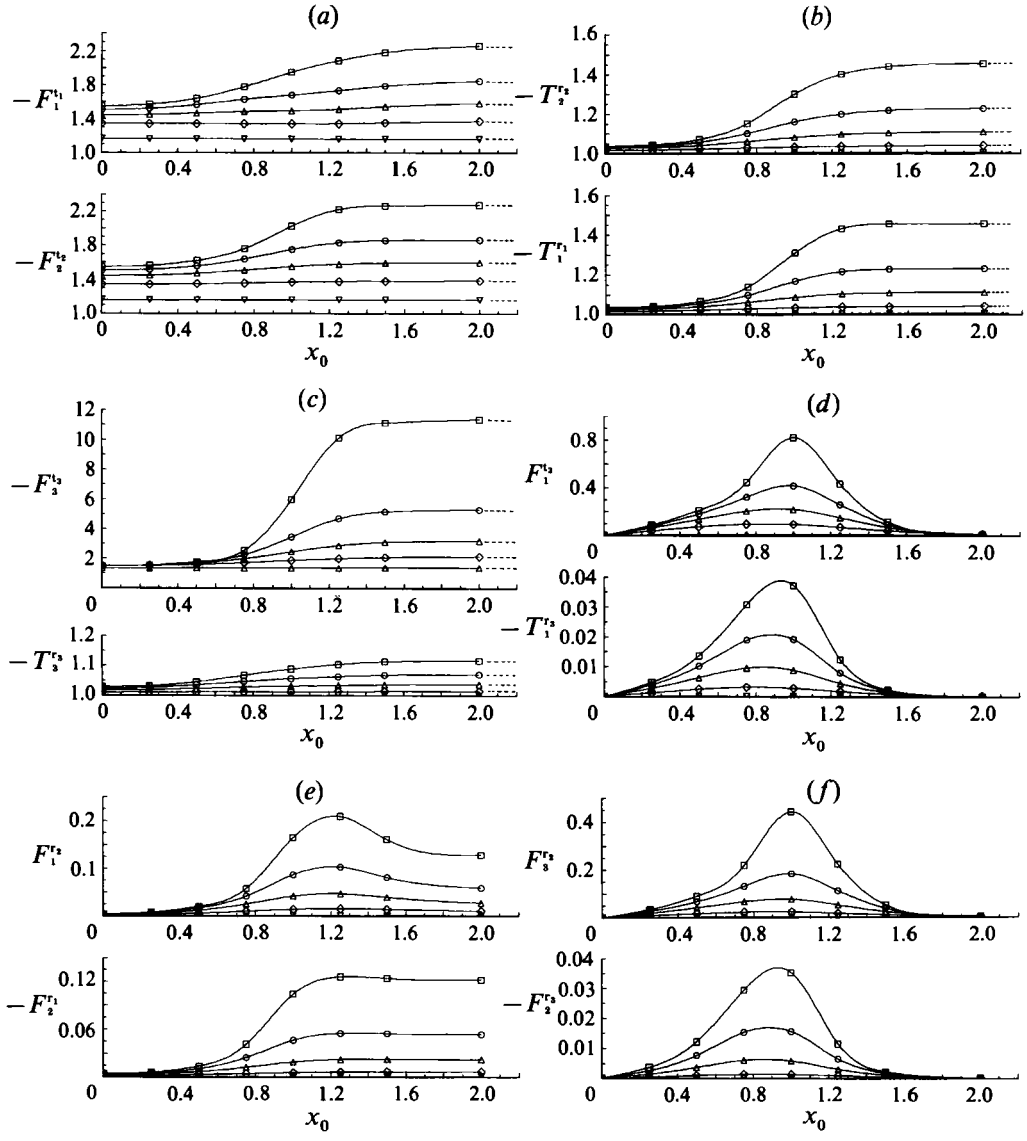

FIGURE 3. Non-dimensional resistance coefficients for the components of a force or a torque exerted on a sphere with dimensionless radius $a = \frac{1}{2}$ translating or rotating in a quiescent fluid: □, $z_0/a = 1.1$; ○, $z_0/a = 1.25$; △, $z_0/a = 1.5$; ◇, $z_0/a = 2.0$; ▽, $z_0/a = 4.0$; ----, the solutions of Brenner (1961): (*a*) $-F_1^{t_1}$ and $-F_2^{t_2}$, (*b*) $-T_2^{r_2}$ and $-T_1^{r_1}$, (*c*) $-F_3^{t_3}$ and $-T_3^{r_3}$, (*d*) $F_1^{t_3}$ and $-T_1^{r_3}$, (*e*) $F_1^{r_2}$ and $-F_2^{r_1}$, (*f*) $F_3^{r_2}$ and $-F_2^{r_3}$.

are much larger for this coefficient. In contrast, $T_3^{r_3}$ is smaller than $T_1^{r_1}$ and $T_2^{r_2}$, since the resistance of a sphere rotating about the z-axis is less than when it is rotating about the x- and y-axes.

The cross-coupling coefficients $F_1^{t_3}$, $F_3^{r_2}$, $F_1^{r_2}$, $-F_2^{r_1}$, $-F_2^{r_3}$ and $-T_1^{r_3}$ are presented in figure 3(*d–f*) for $a = \frac{1}{2}$. Note that, in view of (2.31), $F_1^{t_3} = F_3^{t_1}$ and $T_1^{r_3} = T_3^{r_1}$, and that $T_1^{t_2}$, $T_2^{t_1}$, $T_2^{t_3}$ and $T_3^{t_2}$ are related to $F_2^{r_1}$, $F_1^{r_2}$, $F_3^{r_2}$ and $F_2^{r_3}$ in that order. Also, $F_3^{r_2} \neq -F_2^{r_3}$ and $F_1^{r_2} \neq F_2^{r_1}$, even though when plotted *vs.* x_0 for fixed z_0/a the curves for these coefficients are similar. It is seen that the curves for the coefficients listed above have two characteristics. Specifically, $F_1^{t_3}$, $F_3^{r_2}$, $F_2^{r_3}$ and $-T_1^{r_3}$ vanish at the orifice axis and

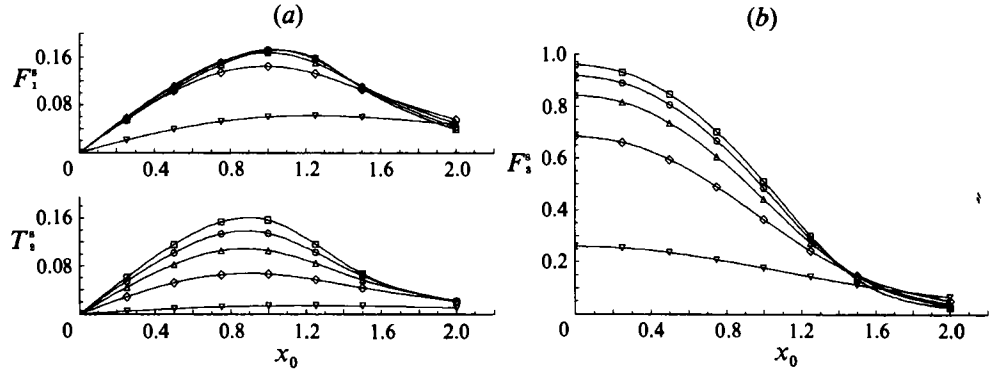

FIGURE 4. Non-dimensional resistance coefficients for the components of a force or a torque acting on a sphere with dimensionless radius $a = \frac{1}{2}$ held fixed in a Sampson flow. Symbols as in figure 3. (*a*) F_1^s and T_2^s, (*b*) F_3^s.

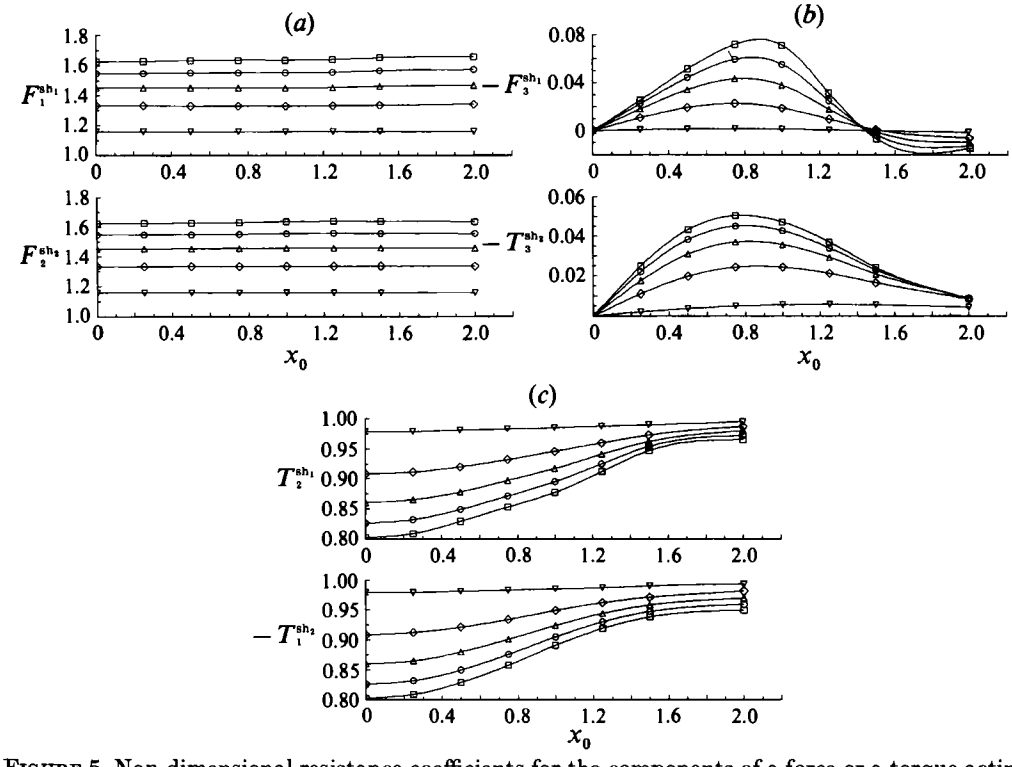

FIGURE 5. Non-dimensional resistance coefficients for the components of a force or a torque acting on a sphere with dimensionless radius $a = \frac{1}{2}$ rigidly held fixed in shear flow 1 and shear flow 2. Symbols as in figure 3. (*a*) $F_1^{sh_1}$ and $F_2^{sh_2}$, (*b*) $-F_3^{sh_1}$ and $-T_3^{sh_2}$, (*c*) $T_2^{sh_1}$ and $-T_1^{sh_2}$.

also as $x_0 \to \infty$, and attain their maximum value in the vicinity of $x_0 = 1.0$, where $F_1^{t_3}$ and $F_3^{r_2}$ are $O(1)$, whereas $-F_2^{r_3}$ and $-T_1^{r_3}$ are one order of magnitude smaller. In contrast, $F_1^{r_2}$ and $-F_2^{r_1}$ are small but non-zero at $x_0 = 0$, both attain their maximum near $x_0 = 1.2$, and, for $x_0 > 2$, approach the finite values given in Goldman *et al.* (1967*a*, *b*) for the rotation of a sphere above an infinite plane wall.

The resistance coefficients F_1^s, F_3^s and T_2^s for the Sampson flow past a fixed sphere, which play an important role in the sphere entrance problem when q is large, are plotted in figure 4 (*a*, *b*). As shown in figure (*b*), F_3^s is of order unity in the vicinity of

	$F_1^{t_1}$				$F_2^{t_2}$			
z_0/a	$x_0/b(z_0)=0$	0.25	0.50	0.75	0	0.25	0.50	0.75
0	−1.763	−1.785	−1.860	−2.027	−1.763	−1.776	−1.821	−1.920
0.5	−1.705	−1.726	−1.798	−1.961	−1.705	−1.719	−1.763	−1.863
1.0	−1.575	−1.603	−1.700	−1.933	−1.575	−1.595	−1.670	−1.871

	$F_3^{t_3}$				$T_1^{r_1}$			
z_0/a	$x_0/b(z_0)=0$	0.25	0.50	0.75	0	0.25	0.50	0.75
0	−1.364	−1.377	−1.420	−1.530	−1.056	−1.059	−1.069	−1.094
0.5	−1.398	−1.415	−1.479	−1.644	−1.051	−1.054	−1.066	−1.096
1.0	−1.459	−1.516	−1.767	−2.843	−1.039	−1.046	−1.075	−1.181

	$T_2^{r_2}$				$T_3^{r_3}$			
z_0/a	$x_0/b(z_0)=0$	0.25	0.50	0.75	0	0.25	0.50	0.75
0	−1.056	−1.061	−1.080	−1.134	−1.055	−1.059	−1.075	−1.115
0.5	−1.051	−1.056	−1.075	−1.130	−1.046	−1.051	−1.065	−1.101
1.0	−1.039	−1.048	−1.085	−1.210	−1.031	−1.036	−1.055	−1.091

	$F_1^{t_3}$				$F_2^{r_1}$			
z_0/a	$x_0/b(z_0)=0$	0.25	0.50	0.75	0	0.25	0.50	0.75
0	0	0	0	0	0	0	0	0
0.5	0	0.0402	0.0927	0.184	−0.0042	−0.00485	−0.00768	−0.0175
1.0	0	0.0909	0.233	0.576	−0.0050	−0.00674	−0.0165	−0.0646

	$F_1^{r_2}$				$F_2^{r_3}$			
z_0/a	$x_0/b(z_0)=0$	0.25	0.50	0.75	0	0.25	0.50	0.75
0	0	0	0	0	0	−0.00630	−0.0174	−0.0461
0.5	0.0042	0.00511	0.00845	0.0171	0	−0.00534	−0.0152	−0.0411
1.0	0.0050	0.00814	0.0221	0.0781	0	−0.00472	−0.0167	−0.0495

	$F_3^{r_2}$				$T_1^{r_3}$			
z_0/a	$x_0/b(z_0)=0$	0.25	0.50	0.75	0	0.25	0.50	0.75
0	0	0.0354	0.0839	0.179	0	0	0	0
0.5	0	0.0339	0.0814	0.178	0	−0.00271	−0.00725	−0.0185
1.0	0	0.0532	0.182	0.321	0	−0.00522	−0.0164	−0.0454

	$F_1^{sh_1}$				$F_2^{sh_2}$			
z_0/a	$x_0/b(z_0)=0$	0.25	0.50	0.75	0	0.25	0.50	0.75
0	0.396	0.396	0.398	0.400	0.396	0.395	0.393	0.391
0.5	0.610	0.611	0.613	0.617	0.610	0.610	0.609	0.609
1.0	0.846	0.847	0.851	0.853	0.846	0.846	0.847	0.849

	$F_3^{sh_1}$				$T_1^{sh_2}$			
z_0/a	$x_0/b(z_0)=0$	0.25	0.50	0.75	0	0.25	0.50	0.75
0	0	−0.00292	−0.00638	−0.0111	−0.523	−0.524	−0.526	−0.532
0.5	0	−0.00564	−0.0122	−0.0202	−0.671	−0.674	−0.681	−0.695
1.0	0	−0.0138	−0.0286	−0.0406	−0.784	−0.791	−0.813	−0.844

TABLE 8. Continued over

$T_2^{sh_1}$

z_0/a	$x_0/b(z_0)=0$	0.25	0.50	0.75
0	0.523	0.524	0.529	0.538
0.5	0.671	0.674	0.683	0.699
1.0	0.784	0.792	0.813	0.838

$T_3^{sh_2}$

0	−0.0241	−0.0479	−0.0700
0	−0.0224	−0.0435	−0.0608
0	−0.0271	−0.0470	−0.0541

F_1^s

z_0/a	$x_0/b(z_0)=0$	0.25	0.50	0.75
0	0	0	0	0
0.5	0	0.0182	0.0363	0.0541
1.0	0	0.0526	0.102	0.142

F_3^s

0	0.25	0.50	0.75
1.132	1.125	1.103	1.065
1.093	1.083	1.055	1.006
0.987	0.959	0.871	0.726

T_2^s

z_0/a	$x_0/b(z_0)=0$	0.25	0.50	0.75
0	0	0.0460	0.0927	0.141
0.5	0	0.0477	0.0957	0.144
1.0	0	0.0648	0.125	0.168

TABLE 8. The resistance coefficients for $a = \frac{1}{2}$ when $z_0/a \leqslant 1.1$

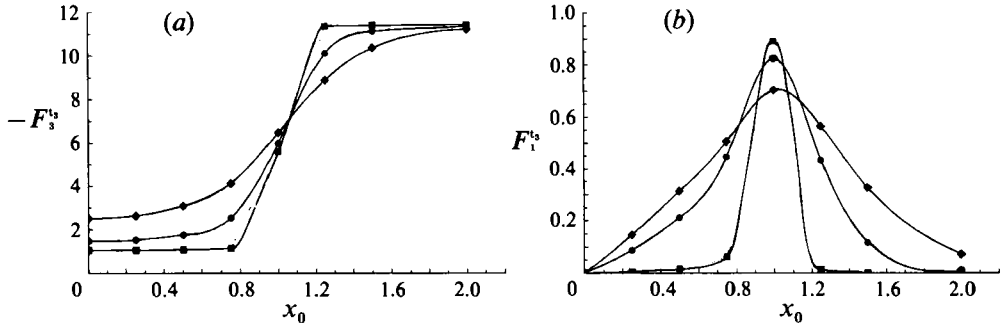

FIGURE 6. Curves showing the influence of the sphere radius along $z_0/a = 1.1$ on $-F_3^{t_3}$ and $F_1^{t_3}$; ■, $a = \frac{1}{10}$; ●, $a = \frac{1}{2}$; ◆, $a = 1$. (a) $-F_3^{t_3}$, (b) $F_1^{t_3}$.

the opening, decreases with increasing x_0 and then approaches zero far from the hole. On the other hand, F_1^s and T_2^s, both of which are an order of magnitude smaller than F_3^s, attain their maximum in the vicinity of $x_0 = 1.0$ and vanish at $x_0 = 0$ or as $x_0 \to \infty$.

The remaining coefficients $F_1^{sh_1}$, $-F_3^{sh_1}$, $T_2^{sh_1}$ for shear flow 1 and $F_2^{sh_2}$, $-T_1^{sh_2}$, $-T_3^{sh_2}$ for shear flow 2 are shown in figure 5(a–c) for $a = \frac{1}{2}$. It is interesting to note that the presence of the orifice has only a small influence on the background motion of the sphere for a simple shear flow past a plane wall. In fact, the existence of the pore entrance has a negligible effect on $F_1^{sh_1}$ and $F_2^{sh_2}$, in accord with the observation that the streamlines for the simple shear flow past an orifice in a plane wall do not deviate significantly from those of the undisturbed shear flow. On the other hand, the z-component of the force, $F_3^{sh_1}$, which exerts some influence on the sphere trajectory in the vicinity of the orifice for the case of small q, attains a small value with a maximum of 0.08 for $z_0/a = 1.1$.

A summary of the values of the coefficients for $a = \frac{1}{2}$ when the sphere intersects the pore opening are given in table 8.

Owing to space limitations, we present in figure 6(*a*, *b*) only the results for $F_3^{t_3}$ and $F_1^{t_3}$ for two other sphere radii; $a = \frac{1}{10}$ and 1. As one would have anticipated, the region of influence of the orifice edge on the coefficients depends on both z_0/a and a in a complicated manner. One notes, however, that the maximum value of $F_1^{t_3}$ is relatively insensitive to the sphere radius a and depends primarily on z_0/a, whereas the width of the region of influence of the orifice edge is affected primarily by the sphere radius.

The complete data and figures for all the resistance coefficients for $a = \frac{1}{10}, \frac{1}{4}, \frac{1}{2}, \frac{3}{4}$ and 1 and can be obtained from the authors on request.

4. Particle screening effects

In this section we shall use the results for the twenty-seven force and torque coefficients described in §3.2 to study the motion of a neutrally buoyant sphere approaching an orifice in a combined Sampson and shear flow, and, in particular, to determine the particle trajectories, the particle capture tube and the particle screening effect. First, for a neutrally buoyant particle and for the case of zero Stokes number, all the forces and torques in (2.29) and (2.30) will vanish, thereby leading to six equations for the six unknown velocity components U_i and ω_i. In fact, the set of three equations for U_1, U_3 and ω_2 resulting from (2.29) by setting $F_1 = F_3 = T_2 = 0$ are decoupled from the corresponding equations for U_2, ω_1 and ω_3 obtained from (2.30) by setting $F_2 = T_1 = T_3 = 0$, and hence each of the two sets can be solved separately. Rewriting these two sets of equations in matrix form we, therefore, have that

$$\boldsymbol{C}_{\mathrm{s}} \boldsymbol{X}_{\mathrm{s}} = V_{z_0}^{\mathrm{s}} \boldsymbol{D}_{\mathrm{s}}^{\mathrm{s}} + G\cos\alpha \boldsymbol{D}_{\mathrm{s}}^{\mathrm{sh}_1}, \tag{4.1}$$

$$\boldsymbol{C}_{\mathrm{a}} \boldsymbol{X}_{\mathrm{a}} = G\sin\alpha \boldsymbol{D}_{\mathrm{a}}^{\mathrm{sh}_2}, \tag{4.2}$$

where

$$\left.\begin{aligned} \boldsymbol{C}_{\mathrm{s}} &= \begin{bmatrix} F_1^{t_1} & F_1^{t_3} & F_1^{r_2} \\ F_3^{t_1} & F_3^{t_3} & F_3^{r_2} \\ T_2^{t_1} & T_2^{t_3} & T_2^{r_2} \end{bmatrix}, \quad \boldsymbol{X}_{\mathrm{s}} = \begin{bmatrix} U_1 \\ U_3 \\ a\omega_2 \end{bmatrix}, \quad \boldsymbol{D}_{\mathrm{s}}^{\mathrm{s}} = \begin{bmatrix} -F_1^{\mathrm{s}} \\ -F_3^{\mathrm{s}} \\ -T_2^{\mathrm{s}} \end{bmatrix}, \quad \boldsymbol{D}_{\mathrm{s}}^{\mathrm{sh}_1} = \begin{bmatrix} -z_0 F_1^{\mathrm{sh}_1} \\ -z_0 F_3^{\mathrm{sh}_1} \\ -\frac{1}{2}aT_2^{\mathrm{sh}_1} \end{bmatrix}; \\ \boldsymbol{C}_{\mathrm{a}} &= \begin{bmatrix} F_2^{t_2} & F_2^{r_1} & F_2^{r_3} \\ T_1^{t_2} & T_1^{r_1} & T_1^{r_3} \\ T_3^{t_2} & T_3^{r_1} & T_3^{r_3} \end{bmatrix}, \quad \boldsymbol{X}_{\mathrm{a}} = \begin{bmatrix} U_2 \\ a\omega_1 \\ a\omega_3 \end{bmatrix}, \quad \boldsymbol{D}_{\mathrm{a}}^{\mathrm{sh}_2} = \begin{bmatrix} z_0 F_2^{\mathrm{sh}_2} \\ \frac{1}{2}aT_1^{\mathrm{sh}_2} \\ \frac{1}{2}aT_3^{\mathrm{sh}_2} \end{bmatrix}. \end{aligned}\right\} \tag{4.3}$$

The solution of (4.1) and (4.2) can be written in the dimensionless form

$$\boldsymbol{X}_{\mathrm{s}}/G = -3Q\boldsymbol{X}_{\mathrm{s}}^{\mathrm{s}} + \cos\alpha \boldsymbol{X}_{\mathrm{s}}^{\mathrm{sh}_1}, \tag{4.4}$$

$$\boldsymbol{X}_{\mathrm{a}}/G = \sin\alpha \boldsymbol{X}_{\mathrm{a}}^{\mathrm{sh}_2}, \tag{4.5}$$

where G is defined in (2.8) and

$$Q = q/(2\pi G) \tag{4.6}$$

is a dimensionless suction parameter related to the fluid velocity at the pore centre from (2.10). The symbols $\boldsymbol{X}_{\mathrm{s}}^{\mathrm{s}}$, $\boldsymbol{X}_{\mathrm{s}}^{\mathrm{sh}_1}$ and $\boldsymbol{X}_{\mathrm{a}}^{\mathrm{sh}_2}$ denote the vectors

$$\boldsymbol{X}_{\mathrm{s}}^{\mathrm{s}} = (U_1^{\mathrm{s}}, U_3^{\mathrm{s}}, a\omega_2^{\mathrm{s}})^{\mathrm{T}}, \quad \boldsymbol{X}_{\mathrm{s}}^{\mathrm{sh}_1} = (U_1^{\mathrm{sh}_1}, U_3^{\mathrm{sh}_1}, a\omega_2^{\mathrm{sh}_1})^{\mathrm{T}}, \quad \boldsymbol{X}_{\mathrm{a}}^{\mathrm{sh}_2} = (U_2^{\mathrm{sh}_2}, a\omega_1^{\mathrm{sh}_2}, a\omega_3^{\mathrm{sh}_2})^{\mathrm{T}} \tag{4.7}$$

obtained from

$$\boldsymbol{C}_{\mathrm{s}} \boldsymbol{X}_{\mathrm{s}}^{\mathrm{s}} = \boldsymbol{D}_{\mathrm{s}}^{\mathrm{s}}, \quad \boldsymbol{C}_{\mathrm{s}} \boldsymbol{X}_{\mathrm{s}}^{\mathrm{sh}_1} = \boldsymbol{D}_{\mathrm{s}}^{\mathrm{sh}_1}, \quad \boldsymbol{C}_{\mathrm{a}} \boldsymbol{X}_{\mathrm{a}}^{\mathrm{sh}_2} = \boldsymbol{D}_{\mathrm{a}}^{\mathrm{sh}_2}, \tag{4.8}$$

corresponding to the Sampson flow and the two shear flows, where the superscript T

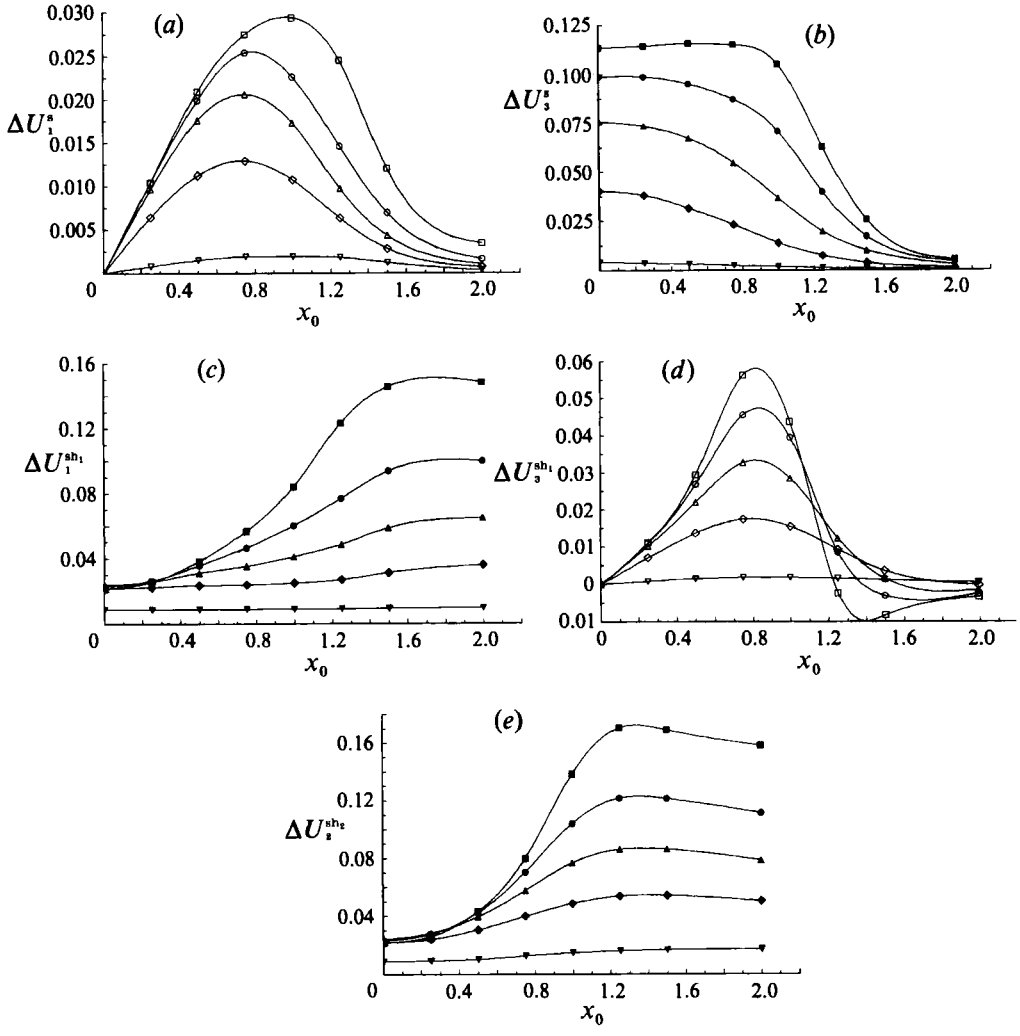

FIGURE 7. The difference in velocity of the undisturbed fluid at the sphere centre and that of the neutrally buoyant sphere with $a = \frac{1}{2}$ for Sampson flow and shear flows 1 and 2. Symbols as in figure 3. (*a*) ΔU_1^s, (*b*) ΔU_3^s, (*c*) $\Delta U_1^{sh_1}$, (*d*) $\Delta U_3^{sh_1}$, (*e*) $\Delta U_2^{sh_2}$.

denotes the transpose of the row matrix. On setting $G = 1$, without loss of generality, we therefore obtain from (4.4) and (4.5)

$$U_1 = -3QU_1^s + \cos\alpha U_1^{sh_1}, \quad U_3 = -3QU_3^s + \cos\alpha U_3^{sh_1}, \quad U_2 = \sin\alpha U_2^{sh_2}. \tag{4.9}$$

It is clear then that, for $G = 1$, the particle velocity components U_i can be determined, for any Q and azimuthal angle α, from (4.9), once U_1^s, U_3^s, $U_1^{sh_1}$, $U_3^{sh_1}$ and $U_2^{sh_2}$ have been evaluated.

The numerical procedure for determining the particle trajectory equations was formulated as follows:

(i) As described previously, the twenty-seven resistance coefficients are calculated at 74 nodal points in the flow field. At each node, (4.8) is then solved to determine U_1^s, U_3^s, $U_1^{sh_1}$, $U_3^{sh_1}$ and $U_2^{sh_2}$.

(ii) The coordinates of the sphere centre are now recast in the new Cartesian system (x, y, z) using (2.1), (2.2) and (2.3).

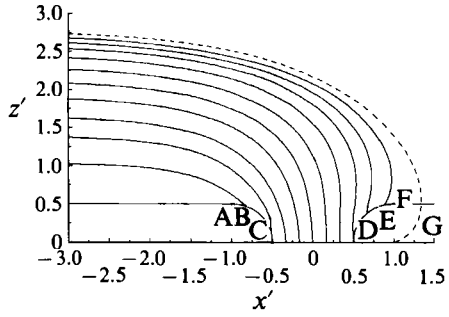

FIGURE 8. Particle trajectories lying within the particle capture tube in the $y' = 0$ plane for $a = \frac{1}{2}$ and $Q = 2$. Dashed line: limiting streamline of the corresponding fluid capture tube.

(iii) Using spline interpolation in two dimensions, values for U_1^{s}, U_3^{s}, $U_1^{\mathrm{sh}_1}$, $U_3^{\mathrm{sh}_1}$ and $U_2^{\mathrm{sh}_2}$ are obtained at any point in the (x, z)-plane using the nodal solutions in step (i). Also the particle velocity is required to vanish as it touches the plane wall or the rim of the hole.

(iv) U_t is now calculated for any Q and α using (4.9).

(v) The transformation formulae

$$U_{x'} = U_1 \cos\alpha - U_2 \sin\alpha, \quad U_{y'} = U_1 \sin\alpha + U_2 \cos\alpha \tag{4.10}$$

are used next to find $U_{x'}$, $U_{y'}$ and $U_{z'}$ at (x', y', z').

(vi) Finally, the trajectories of the sphere are computed by numerically integrating the ordinary differential equations

$$\frac{\mathrm{d}x'}{\mathrm{d}s'} = \frac{U_{x'}}{U}, \quad \frac{\mathrm{d}y'}{\mathrm{d}s'} = \frac{U_{y'}}{U}, \quad \frac{\mathrm{d}z'}{\mathrm{d}s'} = \frac{U_{z'}}{U}, \tag{4.11}$$

where (x', y', z') refers to the sphere centre and $U = |\boldsymbol{U}|$.

Before describing how the shape of the particle capture tube was determined, we first present the results for the difference in the velocity of the undisturbed fluid at the sphere centre and that of the neutrally buoyant sphere for $a = \frac{1}{2}$, by showing in figure 7 (*a–e*) the differences ΔU_1^{s}, ΔU_3^{s}, $\Delta U_1^{\mathrm{sh}_1}$, $\Delta U_2^{\mathrm{sh}_1}$ and $\Delta U_2^{\mathrm{sh}_2}$ at various locations x_0 and z_0. It is seen from these figures that all the particle velocities are always smaller than or equal to the corresponding fluid velocities except for $U_3^{\mathrm{sh}_1}$, where $\Delta U_3^{\mathrm{sh}_1}$ changes in sign as the rim is approached. The slip between the fluid and particle associated with $\Delta U_1^{\mathrm{sh}_1}$ makes an important contribution to the concentration defect described later.

Of special interest are the dividing particle trajectories which separate the particles entering the pore from those continuing downstream in the main tube. The surface formed by all these trajectories enclose a volume, which defines the particle capture tube.

Before considering this particle capture tube, let us first examine the particle trajectories in the $y' = 0$ plane. A representative solution for $a = \frac{1}{2}$ and $Q = 2$ is shown in figure 8 where the curves ABC and DEF depict the steric exclusion boundary for the sphere centre. One observes that there is a finite range of upstream particle trajectories that converge on the boundary ABC, and which represent trajectories of spheres that almost touch the wall and then essentially roll into the hole. This behaviour was observed for pure Sampson flow in Dagan *et al.* (1983). On the downstream side, two limiting curves are shown, one solid and one dashed, of which the latter is the dividing streamline of the fluid phase. Note that it impacts the wall at point G on the rim ($x = 1$). This is to be expected from the fact that the shear

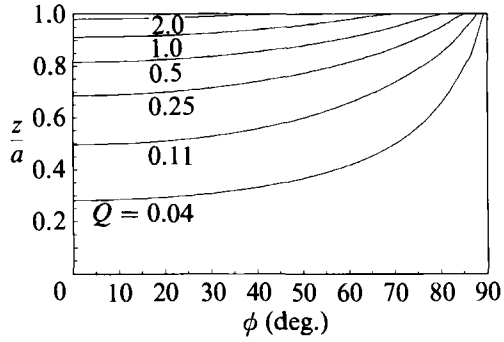

FIGURE 9. The critical curves for different values of Q when $a = \frac{1}{2}$.

stress of the pure Sampson flow vanishes everywhere along the solid plate and that the corresponding shear stress of the pure shear flow is positive. Lying inside this dividing streamline in the plane of symmetry is the upstream limiting particle trajectory, which intersects the downstream exclusion boundary DEF at point E. The location of point E changes with Q, a, and, as we shall describe shortly, the angle ϕ measured from the pore centre, where $\phi = 0$ is the symmetry plane.

To determine point E we examine the tangential component V_τ of the particle velocity at a negligible distance ϵ' from the exclusion curve DEF measured along the radius from the downstream rim. The criterion for particle capture is given by the condition

$$\left.\begin{aligned} V_\tau < 0: &\quad \text{the particle will roll into the hole,} \\ V_\tau > 0: &\quad \text{the particle will be carried downstream,} \end{aligned}\right\} \tag{4.12}$$

and, thus, the downstream separation trajectory is defined by the condition $V_\tau = 0$.

Numerical experiments have shown that the results are insensitive to the value of ϵ' in that almost the same results are obtained whether ϵ' is set equal to 5×10^{-3} or 10^{-1}. As expected, numerical calculations show that all trajectories originating off the plane of symmetry which impact the rim in the range $\frac{1}{2}\pi \leqslant \phi \leqslant \pi$ will enter the pore. In contrast, for spheres impacting the rim in the range $0 \leqslant \phi \leqslant \frac{1}{2}\pi$ there is a critical curve defined by $V_\tau = 0$ which varies with Q and a and lies on the surface generated by rotating the arc DEF in figure 8 about the z-axis. The special case $a = \frac{1}{2}$ is shown in figure 9. It is seen that, for $Q > 2$, the point E in figure 8 approaches the point F and that the critical curve finally coincides with the horizontal line $z/a = 1$. In fact, for large values of the suction parameter Q, the sphere first comes close to the wall downstream of the rim and then rolls backwards into the hole. On the other hand, when the suction is weak, the sphere will also roll backwards into the hole, if it is captured, but the critical curve lies upstream of $\rho = 1$. In addition, spheres, impacting the rim above the critical curve will roll out along the rim. Thus, for each value of a, there is a minimum value of Q which must be exceeded if any particles are to enter the hole. Note that, for $a = \frac{1}{2}$, $Q_{\min} = 0.04$, which is slightly larger than the value $Q_{\min} = 0.0305$ found in Yan *et al.* (1991*a*) from the pure skimming solution.

The upstream particle capture tube is determined by integrating equation (4.11) backwards starting from a point along the critical curve for $V_\tau = 0$ in the region $0 \leqslant \phi \leqslant \frac{1}{2}\pi$, and from a point along the half-circle $\rho = 1$, $z'/a = 1$ in the region $\frac{1}{2}\pi \leqslant \phi \leqslant \pi$. The surface formed by all dividing trajectories generates both the particle capture tube and the upstream capture tube cross-section. This numerical integration has been performed for two particle sizes ($a = \frac{1}{2}$ and $\frac{3}{4}$) and for a range of

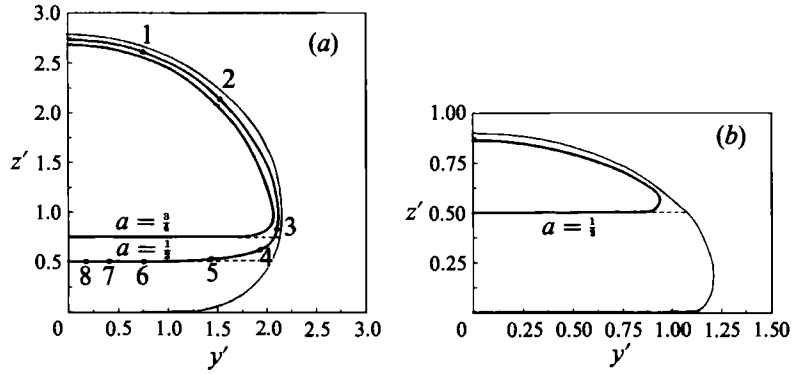

FIGURE 10. Comparison between the far-upstream cross-section shapes of the particle capture tube (bold lines) and those of the fluid capture tube (thin lines). Numbers on upstream particle cross-section for $a = \frac{1}{2}$ correspond to the upstream origin of the particle trajectories shown in figure 11. (*a*) $Q = 2$, $a = \frac{1}{2}$, $a = \frac{3}{4}$; (*b*) $Q = 0.11$, $a = \frac{1}{2}$.

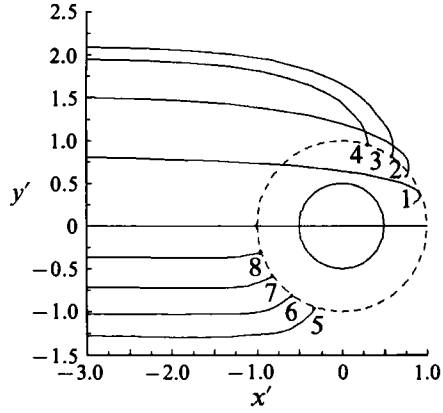

FIGURE 11.The projection of the particle tube surface on the (x', y')-plane for $a = \frac{1}{2}$ and $Q = 2$ (also see caption of figure 10).

suction flow rates $0.04 \leqslant Q \leqslant 5$. Representative upstream capture tube cross-sections for $a = \frac{1}{2}$ and $\frac{3}{4}$ and $Q = 0.11$ and 2 are plotted in figure 10(*a*, *b*). Also shown for comparison are the corresponding upstream cross-sectional shapes of the fluid capture tubes, where the particle exclusion layers, the horizontal dashed lines in these figures, account for the fluid skimming effect. It is evident that the particle and fluid capture tubes have quite different cross-sectional shapes and, that, at any point given location, the particle capture tube always lies within the fluid capture tube. In addition, the sphere and the fluid have different velocities due to the hydrodynamic interaction of the sphere with the wall and with the orifice entrance geometry, which causes the particle to move slower than the surrounding fluid, as shown previously in figure 7. These combined mechanisms are responsible for the particle screening effect. A plan view of the particle trajectories in the (x', y')-plane originating at different locations along the upstream particle capture tube cross-section, which are numbered in sequence for the $Q = 2$ solution in figure 10(*a*), are shown in figure 11.

We next consider the concentration defect at the exit of the pore on the basis of the results given above, taking into consideration both the fluid skimming and particle screening effects. We suppose that the particle concentration at upstream

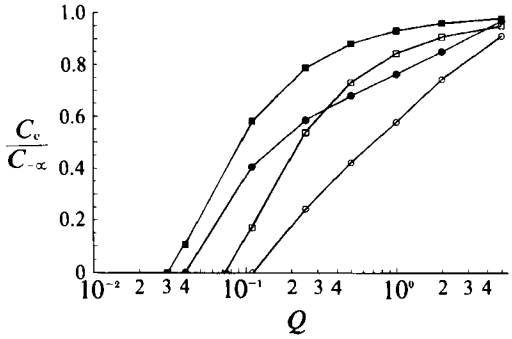

FIGURE 12. The effect of the particle screening and the fluid skimming on the concentration defect at the pore exit (○, due to both the particle screening and the fluid skimming effects; □, due to the fluid skimming effect alone; the solid symbols, $a = \frac{1}{2}$, the open symbols, $a = \frac{3}{4}$.

infinity has the uniform value $C_{-\infty}$. Then, if $C_{-\infty} \ll 1$, the flux of pure fluid into the orifice is $2\pi QG$, while the corresponding particle flux is $2\pi C_{-\infty} GQ_p$, where

$$2\pi Q_p = \int U_{x'} \, dy' \, dz', \tag{4.13}$$

in which $U_{x'}$ is obtained from (4.10) and the integration domain extends over the entire far upstream cross-sectional area of the particle capture tube. Mass conservation for the particle phase requires, however, that the particle flux also equal $2\pi C_e QG$, where C_e is the particle discharge concentration at the pore exit. Thus we obtain

$$\frac{C_e}{C_{-\infty}} = \frac{Q_p}{Q} \quad \text{as} \quad C_{-\infty} \to 0, \tag{4.14}$$

Our results for the concentration defect for this limit are plotted in figure 12, where the lines with the circle symbols correspond to (4.14) with both the particle screening and fluid skimming effects taken into account, while the lines with box symbols are taken from Yan *et al.* (1991*a*) and represent only the fluid skimming effect. It is seen that the concentration defect is enhanced by particle screening and that the pure skimming solution provides an upper bound for $C_e/C_{-\infty}$.

It would be expected that the relative importance of the particle screening effect would increase rapidly as the radius of the particle increases and approaches that of the pore. For these cases, however, the frequent choking of the pore mouth by particles will alter the background fluid flow field significantly and, thus, the hydrodynamic interaction between different particles can no longer be neglected. Unfortunately, our present model is too simplified to be able to describe such cases with any degree of reliability. It should also be noted in passing that our analysis has taken Q, which is related to the flux of the background Sampson flow, as fixed, which is equivalent to fixing the pressure drop across the orifice, whereas the actual flow of fluid through the orifice will decrease as the particle approaches the pore due to the blockage of the opening. This decrease in the flow for a fixed pressure drop is the situation usually encountered in practice.

5. Concluding remarks

In the present paper, the boundary-integral method has been applied to obtain the first solutions for the hydrodynamic interaction of a sphere in a simple shear flow with suction past an infinite wall with a circular side hole. This fully three-

dimensional flow geometry was treated using the Green function developed by Miyazaki & Hasimoto (1984) and further extended in the present analysis. The general approach is applicable for any undisturbed velocity field which does not contain singularities internal to the sphere surface, and includes the two shear flows and the Sampson flow considered in this paper. The numerical results indicate that excellent convergence and high accuracy can be achieved using this procedure with acceptable computational time. Although the integral equation which is solved is of the first kind and is well known to be ill conditioned, the numerical calculations indicate that, as previously demonstrated by Youngren & Acrivos (1975) for unbounded flows, no difficulties are encountered with respect to convergence and stability for this more complicated bounded flow. The proposed method appears to be the most reliable and accurate of the various numerical schemes that have been proposed thus far for treating particle entrance problems. The basic approach can also be extended to include rigid particles of arbitrary shape and deformable fluid droplets. Solutions can also be obtained for the more difficult cases where the sphere can impact the rim of the hole or intersect the plane of the hole. These solutions are crucial in defining the upstream particle capture tube.

In concluding this paper, we wish to make a few comments concerning the blood flow problem that provided the motivation for this study. In Yan *et al.* (1991*b*), an approximate procedure is presented for extending the theory for fluid skimming to an upstream Poiseuille flow in a parent vessel with a small circular side branch in the low-Q limit. It is shown that, for flows typical of microvascular bifurcations *in vivo*, Q varies from being negligible to 0.2 with a mean value of 0.1. The present numerical solutions show that the discharge hematocrits predicted in Yan *et al.* (1991*a*) provide an upper bound and that, if particle screening were included, C_e could be significantly lower. Further, it is clear from figure 12, that particle screening increases the minimum value of Q which must be exceeded if any cells are to enter the side branch. Examination of figure 12 reveals furthermore that the maximum deviation between the exit concentration predicted by the pure fluid skimming analysis and the present theory for both the particle screening and the fluid skimming for a dilute suspension occurs roughly at $Q = 0.5$ for the two values of a shown. For $Q = 0.1$ and $a = \frac{1}{2}$ the deviation in the predicted exit concentration is about 30% and then increases as a increases, while, for $a = \frac{3}{4}$ the minimum value of Q for cells to enter the side branch would exceed $Q = 0.1$. The close fitting limit where cells could still enter the side branch would thus appear to lie outside the range of Q encountered in the microcirculation *in vivo*, but in other non-biological applications, such as cross-flow filters, the close fitting limit could be of special interest since it is clear from the results in figure 12 that the difference between the pure skimming and both the particle screening and the fluid skimming results could increase very substantially for Q of $O(1)$. We also mention that typical hematocrits in the blood circulation are of the order of 40% and thus are far greater than the dilute limit considered herein. For this high concentration there is a cell-free layer near the wall, but in the core of the flow the two phases will have a much smaller slip velocity than predicted by figure 7(*c*). On this basis, one would anticipate, therefore, that the discharge hematocrit H_D would lie somewhere between the results for pure fluid skimming and the dilute theory for both the particle screening and the fluid skimming predicted herein. On the other hand, since the increase in the hematocrit concentration near the entrance to the orifice would be expected to lead to a further reduction in H_D, it is not clear at this stage of the analysis how these two opposing effects, when combined, would affect the hematocrit defect in a typical biological system. Finally, while red cells

are highly deformable biconcave disks, the much more infrequent white cells are very nearly spherical and are present in concentrations that are within the range of the dilute theory in which the background undisturbed flow can be approximated by a Poiseuille tube flow. The extension of the present theory to this case is currently being explored.

Since the three-dimensional hydrodynamic resistance coefficients for a finite sphere immersed in a shear flow with suction past an infinite wall containing a hole are a fundamental input for all problems involving particle entrance phenomena, it is anticipated that the method and the results presented in this paper will be useful in many applications other than the blood flow problem that was the motivation for this study.

This research was supported by the National Science Foundation under grant CTS-8803116 and by the State of New York under its Einstein Chair Program.

Appendix

When $\theta = \theta_m$ and $\phi = \phi_m$, the following integral becomes singular:

$$I = \iint_{S_p} G^{ij}(x, y)\, \mathrm{d}Sy, \tag{A 1}$$

where θ_m and ϕ_m are the corresponding values of θ and ϕ at the centre of the element. To evaluate the above integral, the region of integration is divided into five subregions:

$$I = \int_{\theta_1}^{\theta_m-\epsilon_\theta}\int_{\phi_1}^{\phi_3} + \int_{\theta_m+\epsilon_\theta}^{\theta_2}\int_{\phi_1}^{\phi_3} + \int_{\theta_m-\epsilon_\theta}^{\theta_m+\epsilon_\theta}\int_{\phi_1}^{\phi_m-\epsilon_\phi} + \int_{\theta_m-\epsilon_\theta}^{\theta_m+\epsilon_\theta}\int_{\phi_m+\epsilon_\phi}^{\phi_3} + \int_{\theta_m-\epsilon_\theta}^{\theta_m+\epsilon_\theta}\int_{\phi_m-\epsilon_\phi}^{\phi_m+\epsilon_\phi}, \tag{A 2}$$

where θ_1, θ_2 and ϕ_1, ϕ_3 are the corresponding values at four sides of the element, and

$$\epsilon_\theta = \epsilon/a, \quad \epsilon_\phi = \epsilon/(a \sin\theta_m). \tag{A 3}$$

The first four integrals on the right-hand side of (A 2) are regular and can be evaluated by means of an 8×8 composite Gaussian quadrature formula, while the last one is singular. Following the approach by Youngren & Acrivos (1975), we treat the small region around the singularity as a flat plane and use the formula presented in Appendix B of their paper to calculate the last integral analytically.

Rewriting G^{ij} in the following form:

$$8\pi\mu G^{ij} = S^{(1)}_{i,j} + S^{(2)}_{i,j} + S^{(3)}_{i,j}, \tag{A 4}$$

where $S^{(2)}_{i,j} = \boldsymbol{O}_3(\boldsymbol{\Phi}_j), \quad S^{(3)}_{i,j} = \boldsymbol{q}^j,$

$$\begin{aligned} S^{(1)}_{i,j} &= \boldsymbol{O}_j(L) - y_j \boldsymbol{\nabla} L \\ &= -\frac{1}{2}\left(\frac{\delta_{ij}}{R} + \frac{(x_i - y_i)(x_j - y_j)}{R^3}\right)\left(1 + \frac{2}{\pi}\sin^{-1}\left(\frac{\cos[\frac{1}{2}(\eta - \eta_0)]}{\cosh(\frac{1}{2}\omega)}\right)\right) \\ &\quad + \frac{x_j - y_j}{2R}\frac{\partial}{\partial x_i}\left(1 + \frac{2}{\pi}\sin^{-1}\left(\frac{\cos[\frac{1}{2}(\eta - \eta_0)]}{\cosh(\frac{1}{2}\omega)}\right)\right) \\ &\quad + \frac{1}{2}\left(\frac{\delta_{ij}}{R^*} + \frac{(x_i - y_i^*)(x_j - y_j)}{R^{*3}}\right)\left(1 + \frac{2}{\pi}\sin^{-1}\left(\frac{\cos[\frac{1}{2}(\eta - \eta_0)]}{\cosh(\frac{1}{2}\omega)}\right)\right) \\ &\quad - \frac{x_j - y_j}{2R^*}\frac{\partial}{\partial x_i^*}\left(1 + \frac{2}{\pi}\sin^{-1}\left(\frac{\cos[\frac{1}{2}(\eta - \eta_0)]}{\cosh(\frac{1}{2}\omega)}\right)\right) \end{aligned}$$

we obtain after tedious manipulations

$$\int_{\theta_m-\epsilon_\theta}^{\theta_m+\epsilon_\theta}\int_{\phi_m-\epsilon_\phi}^{\phi_m+\epsilon_\phi}(S_{i,j}^{(1)}+S_{i,j}^{(2)}+S_{i,j}^{(3)})\,\mathrm{d}x\,\mathrm{d}y = -K_c\,\epsilon(3\boldsymbol{I}-\boldsymbol{S}) + \bar{K}_c\,\epsilon^2(\boldsymbol{I}-\boldsymbol{S})+\bar{\bar{K}}_c\,\epsilon^2\boldsymbol{I}+4\epsilon^2(S_{i,j}^{(2)}+S_{i,j}^{(3)})_m$$

where $$K_c = 2\ln\frac{\sqrt{2}+1}{\sqrt{2}-1},\quad \bar{K}_c = -\tfrac{1}{2}M_0^2,\quad \bar{\bar{K}}_c = \frac{1}{Z_m}\left(1+\frac{2}{\pi}\sin^{-1}\eta_m\right)$$

$$\boldsymbol{S} = \begin{bmatrix} X_m^2 & X_mY_m & Z_mX_m \\ \frac{1}{a^2}X_mY_m & Y_m^2 & Y_mZ_m \\ Z_mX_m & Y_mZ_m & Z_m^2 \end{bmatrix},\quad \boldsymbol{I} = \begin{bmatrix} 1 & 0 & 0 \\ 0 & 1 & 0 \\ 0 & 0 & 1 \end{bmatrix}.$$

and (X_m, Y_m, Z_m) are the Cartesian coordinates of the point m relative to the origin at the centre of the sphere (cf. figure 2).

As discussed at the end of §2, there is an optimum value of ϵ which provides the best agreement with the known values of the coefficients when the sphere is far from the hole. Optimum values of ϵ for the strong-interaction cases considered are

	10×10	11×11	12×12
$z_0/a = 1.10$	0.05353	0.058823	0.06388
$z_0/a = 1.25$	0.05552	0.061093	
$z_0/a = 1.50$	0.05745	0.063376	

For other cases we have used $\epsilon = 0.1$.

REFERENCES

Blake, J. R. 1971 *Proc. Camb. Phil. Soc.* **70**, 303.

Brenner, H. 1961 *Chem. Engng Sci.* **16**, 242.

Chien, S., Usami, S. & Skalak, R. 1984 In *Handbook of Physiology – The Cardiovascular System IV*, Ch. 6, pp. 217–49. Bethesda, Md: Am. Physiol. Soc.

Cokelet, G. R. 1976 In *Microcirculation* (ed. J. Grayson & W. Zingg), vol. 1, pp. 9–23.

Dagan, Z., Weinbaum, S. & Pfeffer, R. 1982 *J. Fluid Mech.* **117**, 143.

Dagan, Z., Weinbaum, S. & Pfeffer, R. 1983 *Chem. Engng Sci.* **38**, 583.

Davis, A. M. J. 1983 *Intl J. Multiphase Flow* **9**, 575.

Davis, A. M. J. 1991 *Phys. Fluids* A **3**, 478.

Davis, A. M. J., O'Neil, M. E. & Brenner, H. 1981 *J. Fluid Mech.* **103**, 183.

Gaehtgens, P. A. L. & Papenfuss, H. D. 1979 *Bibl. Anat.* **18**, 53.

Gavze, E. 1990 *Intl J. Multiphase Flow* **16**, 529.

Goldman, M. J., Cox, R. G. & Brenner, H. 1967*a* *Chem. Engng Sci.* **22**, 637.

Goldman, M. J., Cox, R. G. & Brenner, H. 1967*b* *Chem. Engng Sci.* **22**, 653.

Happel, J. & Brenner, H. 1973 *Low Reynolds Number Hydrodynamics*, 2nd edn. Noordhoff.

Hasimoto, H. 1981 *J. Phys. Soc. Japan* **50**, 3521.

Kao, J. N., Wang, Y., Pfeffer, R. & Weinbaum, S. 1988 *J. Colloid Interface Sci.* **121**, 543.

Lipowsky, H. H. 1986 In *Microcirculatory Technology*, Ch. 12, pp. 161–78. Academic.

Miyazaki, T. & Hasimoto, H. 1984 *J. Fluid Mech.* **145**, 201.

O'Neill, M. E. 1964 *Mathematika* **11**, 67.

Pries, A. R., Ley, K. & Gaehtgens, P. 1986 *Am. J. Physiol.* **251**, 1324.

Smith, S. H. 1987 *Intl J. Multiphase Flow* **13**, 219.

TUTTY, O. R. 1988 *J. Fluid Mech.* **191**, 79.
WANG, Y. A., KAO, J., WEINBAUM, S. & PFEFFER, R. 1986 *Chem. Engng Sci.* **41**, 2845.
YAN, Z., ACRIVOS, A. & WEINBAUM, S. 1991*a* *J. Fluid Mech.* **229**, 1.
YAN, Z., ACRIVOS, A. & WEINBAUM, S. 1991*b* *Microvasc. Res.* **42**, 17.
YAN, Z., WEINBAUM, S., GANATOS, P. & PFEFFER, R. 1987 *J. Fluid Mech.* **174**, 39.
YAN, Z., WEINBAUM, S. & PFEFFER, R. 1986 *J. Fluid Mech.* **162**, 415.
YOUNGREN, G. K. & ACRIVOS, A. 1975 *J. Fluid Mech.* **69**, 377.